

Assimilating Doppler radar radial velocity and reflectivity observations in the weather research and forecasting model by a proper orthogonal-decomposition-based ensemble, three-dimensional variational assimilation method

Xiaoduo Pan,¹ Xiangjun Tian,² Xin Li,¹ Zhenghui Xie,² Aimei Shao,³ and Chunyan Lu³

Received 23 February 2012; revised 24 July 2012; accepted 24 July 2012; published 11 September 2012.

[1] Doppler radar observations with high spatial and temporal resolution can effectively improve the description of small-scale structures in the initial condition and enhance the mesoscale and microscale model skills of numerical weather prediction (NWP). In this paper, Doppler radar radial velocity and reflectivity are simultaneously assimilated into a weather research and forecasting (WRF) model by a proper orthogonal-decomposition-based ensemble, three-dimensional variational assimilation method (referred to as PODEn3DVar), which therefore forms the PODEn3DVar-based radar assimilation system (referred to as WRF-PODEn3DVar). The main advantages of WRF-PODEn3DVar over the standard WRF-3DVar are that (1) the PODEn3DVar provides flow-dependent covariances through the evolving ensemble of short-range forecasts, and (2) the PODEn3DVar analysis can be obtained directly without an iterative process, which significantly simplifies the assimilation. Results from real data assimilation experiments with the WRF model show that WRF-PODEn3DVar simulation yields better rainfall forecasting than radar retrieval, and radar retrieval is better than the standard WRF-3DVar assimilation, probably because of the flow-dependence character embedded in the WRF-PODEn3DVar.

Citation: Pan, X., X. Tian, X. Li, Z. Xie, A. Shao, and C. Lu (2012), Assimilating Doppler radar radial velocity and reflectivity observations in the weather research and forecasting model by a proper orthogonal-decomposition-based ensemble, three-dimensional variational assimilation method, *J. Geophys. Res.*, 117, D17113, doi:10.1029/2012JD017684.

1. Introduction

[2] Numerical weather prediction (NWP) requires an accurate initial condition—the precise present status of the atmosphere—for models to accurately forecast future weather. Data assimilation is a good strategy for constructing the best possible initial condition for NWP using observational data. Compared with the traditional observational data, Doppler radar observations have become increasingly important for data assimilation for mesoscale or microscale NWP because of their high temporal and spatial resolution. They have been more widely used, and they have been shown to improve weather forecasting accuracy [Meischner, 2005].

[3] Doppler radar-observation data assimilation has been developed since *Gal-Chen* [1978] first proposed an algorithm to combine the use of equations of cloud dynamics and the observed wind from Doppler radar to uniquely determine the density and pressure fluctuations in the anelastic equations. There are two developing stages for Doppler radar-observation variational data assimilation: one is the retrieval of wind and/or thermal fields from Doppler radar observations by variational data assimilation in a simple atmospheric model; the other is the assimilation of Doppler radar observations into a numerical weather prediction (NWP) model directly. The common objective for these two stages is to provide better initial conditions for the forecasting model. In the first stage, *Wolfsberg* [1987] retrieved three-dimensional wind and temperature fields from single Doppler radar radial-velocity observations in a Boussinesq model based on the four-dimensional variational data assimilation (4DVar), which, in a comprehensive and complicated numerical model, presents a hard task in setting up a tangent linear model and its adjoint model of the numerical model in order to obtain the initial variable gradient in the cost function. A few years later, *Kapitza* [1991] examined Doppler radar radial velocity by 4DVar using idealized observation data and a dry, non-hydrostatic, numerical model without considering the background, and they obtained the approximate structure of a thermal column. *Sun et al.* [1991] and *Sun and Crook* [1994] retrieved wind and thermodynamic fields from Doppler radar

¹Cold and Arid Regions Environmental and Engineering Research Institute, Chinese Academy of Sciences, Lanzhou, China.

²State Key Laboratory of Numerical Modeling for Atmospheric Sciences and Geophysical Fluid Dynamics, Institute of Atmospheric Physics, Chinese Academy of Sciences, Beijing, China.

³Key Laboratory for Semi-Arid Climate Change of the Ministry of Education, College of Atmospheric Sciences, Lanzhou University, Lanzhou, China.

Corresponding author: X. Pan, Cold and Arid Regions Environmental and Engineering Research Institute, Chinese Academy of Sciences, Lanzhou 730000, China. (panxiao@lzb.ac.cn)

©2012. American Geophysical Union. All Rights Reserved.
0148-0227/12/2012JD017684

radial-velocity and reflectivity data using a simple cloud model and its adjoint model. Following this, *Sun and Crook* [1997, 1998] used the warm cloud model to retrieve wind and thermodynamic fields from Doppler radar radial-velocity and reflectivity data. Based on the works of *Sun et al.* [1991] and *Sun and Crook* [1994, 1997, 1998], the National Center for Atmospheric Research (NCAR) built the four-dimensional Variational Doppler Radar Analysis System (VDRAS). *Wu et al.* [2000] developed a mixed-phase model in VDRAS that adds the microphysical process of the simple ice phase to the VDRAS; the improved VDRAS can describe all the main characteristics of a deep-convective storm. *Weygandt et al.* [2002a, 2002b] developed a single-Doppler-parameter retrieval technique and applied it to a real-data case to provide initial model conditions for a short-range prediction of a supercell thunderstorm.

[4] In the second stage, *Xiao et al.* [2005] assimilated Doppler radar radial velocity in the fifth-generation Pennsylvania State University-NCAR Mesoscale Model (MM5) to simulate a heavy rainfall event. *Xu et al.* [2006] assimilated Doppler radar data by 4DVar in MM5 to forecast convective rainfall. *Xiao et al.* [2007] assimilated Doppler radar reflectivity in MM5 to simulate Typhoon Rusa, the results show that direct assimilation of Doppler radar observation data can improve the typhoon initialization and improve the prediction of the rainband movement and intensity change. *Xiao and Sun* [2007] assimilated Doppler radar radial-velocity and reflectivity data in the weather research and forecasting (WRF) model known as the Advanced Research WRF (ARW) to evaluate the impact of Doppler radar data assimilation on quantitative precipitation forecasting (QPF).

[5] On the other hand, an ensemble Kalman filter (EnKF) has been increasingly applied to radar-data assimilation. *Snyder and Zhang* [2003] and *Zhang et al.* [2004] assimilated radial-velocity data to improve wind, temperature, and moisture field data for convective storms by EnKF. *Dowell et al.* [2002] and *Tong and Xue* [2005] assimilated radial velocity and reflectivity into a nonhydrostatic, anelastic numerical model by EnKF.

[6] The main objective of this paper is to assimilate Doppler radar radial-velocity and reflectivity data in the WRF model by 3DVar based on the proper orthogonal decomposition (POD) for rainfall forecasting (referred to as WRF-PODEN3DVar hereafter). The POD technique has been shown to be an efficient way to produce an approximate forecast ensemble by the Monte Carlo method in a four-dimensional (4-D) or three-dimensional (3-D) space using a set of base vectors that span the ensemble and capture its spatial structure and temporal evolution [*Tian et al.*, 2008, 2011; *Daescu and Navon*, 2007; *Fang et al.*, 2009]. The potential advantages of WRF-PODEN3DVar over traditional WRF-3DVar are: (1) the PODen3DVar constructs flow-dependent covariances through the evolving ensemble of short-range forecasts, and (2) the PODen3DVar analysis can be obtained directly, without an iterative process, thereby reducing the computational costs.

[7] The paper is organized as follows. The numerical model and its observation operators for Doppler radar radial-velocity and reflectivity data as well as their increments are described in Section 2 along with a brief introduction of POD-based 3DVar. The experimental design, including WRF configuration, traditional WRF-3DVar, Doppler radar

radial-observation data, rainfall retrieval based on Doppler radial observation, and gauge data, are introduced in Section 3. Analysis of sensitivity to ensemble number size and localization radius and a single-observation simulation are performed in Section 4 to test the robustness of the WRF-PODEN3Dvar system. The results and discussion are presented in Section 5, and Section 6 offers conclusions.

2. Methods

2.1. WRF Model and Observation Operators

[8] The numerical model chosen for this study is the WRF-ARW model version 3.1 [*Michalakes et al.*, 1999, 2001], which is a next-generation, mesoscale, numerical weather prediction system that serves both operational and research communities. The use of the WRF system has been reported in a variety of areas, including storm prediction and research, air-quality modeling, wildfire, hurricane and tropical storm prediction, and regional climate and weather prediction [*Michalakes et al.*, 2005].

[9] To assimilate Doppler radar radial-velocity and reflectivity data, the observation operators (\mathbf{H}_Z and \mathbf{H}_V), which link the model states and the radar observations (including data for both the radar reflectivity and radial velocity) are built: \mathbf{H}_Z links Doppler radar reflectivity and WRF-model output, and \mathbf{H}_V links the Doppler radar radial velocity and WRF-model output.

[10] \mathbf{H}_Z is formulated as below (according to *Sun and Crook* [1997, 1998]):

$$Z_e = 2.04 \times 10^4 (\rho q_r)^{1.75} \quad (1)$$

where q_r is the model-predicted rainwater mixing ratio (units of g kg^{-1}), ρ is the density of air, and Z_e is the model-predicted reflectivity (units of $\text{mm}^6 \text{m}^{-3}$), which can be calculated using the model output q_r . In this study, the reflectivity is in units of dBZ, and the $Z_e - q_r$ relation becomes:

$$Z_e = 43.1 + 17.5 \log(q_r). \quad (2)$$

[11] \mathbf{H}_V is expressed as below (according to *Sun and Crook* [1997, 1998]):

$$V = u \frac{x - x_r}{r} + v \frac{y - y_r}{r} + (w - V_{Tm}) \frac{z - z_r}{r}, \quad (3)$$

where u , v and w are the wind velocities, and r is the distance between a grid point (x, y, z) and the radar location (x_r, y_r, z_r) . V_{Tm} is the terminal velocity of the precipitation given by:

$$V_{Tm} = 5.40a(\rho q_r)^{0.125}. \quad (4)$$

[12] The quantity a is a correction factor defined by:

$$a = (p_0/\bar{p})^{0.4}, \quad (5)$$

where \bar{p} is the base-state pressure, and p_0 is the pressure at the ground.

2.2. PODen3DVar

[13] The PODen3DVar is degenerated from PODen4DVar [*Tian et al.*, 2008, 2011] when the time window is set to 1.

The traditional 3DVar optimal increment (\mathbf{x}'_a) is obtained through the minimization of the following incremental format of the standard 3DVar cost function:

$$J(\mathbf{x}') = \frac{1}{2} (\mathbf{x}')^T \mathbf{P}_b^{-1} (\mathbf{x}') + \frac{1}{2} [\mathbf{y}'(\mathbf{x}') - \mathbf{y}'_{obs}]^T \mathbf{R}^{-1} [\mathbf{y}'(\mathbf{x}') - \mathbf{y}'_{obs}] \quad (6)$$

where $\mathbf{x}' = \mathbf{x} - \mathbf{x}_b$ is the perturbation of the background field \mathbf{x}_b at t_0 , and

$$\mathbf{y}' = y(\mathbf{x}_b + \mathbf{x}') - y(\mathbf{x}_b), \quad (7)$$

$$\mathbf{y}'_{obs} = \mathbf{y}_{obs} - y(\mathbf{x}_b), \quad (8)$$

$$y = H(M(\mathbf{x})). \quad (9)$$

[14] Here the superscript T in (6) stands for a transpose, b is the background value, H is the observation operator, and matrices \mathbf{P}_b and \mathbf{R} are the background and observational error covariances, respectively.

[15] Following Tian *et al.* [2011], this ensemble 3DVar method starts from an ensemble of N observation perturbations (OPs) \mathbf{y}' : $\mathbf{y}'_1, \mathbf{y}'_2, \dots, \mathbf{y}'_N$, which are generated by using the observation operator H , the forecast model M and the initial condition (IC) samples \mathbf{x}' : $\mathbf{x}'_1, \mathbf{x}'_2, \dots, \mathbf{x}'_N$. The POD of this OP matrix \mathbf{y}' yields:

$$\mathbf{y}'^T \mathbf{y}' = \mathbf{V} \Lambda^2 \mathbf{V}^T, \quad (10)$$

and

$$\mathbf{P}_y = \mathbf{y}' \mathbf{V}. \quad (11)$$

where Λ is a diagonal matrix of the singular values of \mathbf{y}' , \mathbf{V} is an orthogonal matrix and \mathbf{P}_y is the POD-transformed OP matrix.

[16] Under the linear assumption between the OPs and the model (or state) perturbations (MPs), the MP matrix is transformed as follows:

$$\mathbf{P}_x = \mathbf{x}' \mathbf{V}. \quad (12)$$

[17] The optimal solution \mathbf{x}'_a and its corresponding optimal OP \mathbf{y}'_a can be expressed by the linear combinations of the POD-transformed MPs and OPs, respectively, as follows:

$$\mathbf{x}'_a = \mathbf{P}_x \boldsymbol{\beta}, \quad (13)$$

and

$$\mathbf{y}'_a = \mathbf{P}_y \boldsymbol{\beta}. \quad (14)$$

[18] Substituting (13–14) and the ensemble background covariance $\mathbf{P}_b = \frac{\mathbf{P}_x \mathbf{P}_x^T}{N-1}$ into (6), (\mathbf{P}_x is the POD-transformed MP matrix.) the control variable becomes $\boldsymbol{\beta}$ instead of \mathbf{x}' , so the control variable is expressed explicitly in the cost function:

$$J(\boldsymbol{\beta}) = \frac{1}{2} (N-1) \cdot \boldsymbol{\beta}^T \mathbf{P}_x^T (\mathbf{P}_x^T)^{-1} (\mathbf{P}_x)^{-1} \mathbf{P}_x \boldsymbol{\beta} + \frac{1}{2} (\mathbf{P}_y \boldsymbol{\beta} - \mathbf{y}'_{obs})^T \mathbf{R}^{-1} (\mathbf{P}_y \boldsymbol{\beta} - \mathbf{y}'_{obs}). \quad (15)$$

[19] Through simple calculations (see Tian *et al.* [2011] for more details), the solution for \mathbf{x}'_a is simplified into the following form:

$$\mathbf{x}_a = \mathbf{P}_x \left[(N-1) \mathbf{I} + \mathbf{P}_y^T \mathbf{R}^{-1} \mathbf{P}_y \right]^{-1} \mathbf{P}_y^T \mathbf{R}^{-1} \mathbf{y}'_{obs}. \quad (16)$$

[20] Making $\mathbf{P}_a^* = [(N-1) \mathbf{I} + \mathbf{P}_y^T \mathbf{R}^{-1} \mathbf{P}_y]^{-1}$, the final 3DVar analysis \mathbf{x}_a can be calculated through:

$$\mathbf{x}_a = \mathbf{x}_b + \mathbf{P}_x \mathbf{P}_a^* \mathbf{P}_y^T \mathbf{R}^{-1} \mathbf{y}'_{obs}. \quad (17)$$

[21] Furthermore, the analysis ensemble perturbations \mathbf{X}^a can be updated in a square-root filter way:

$$\mathbf{X}^a = \mathbf{P}_x \left[(N-1) \mathbf{P}_a^* \right]^{\frac{1}{2}}, \quad (18)$$

which makes the PODEn3DVar flow-dependent. Furthermore, an implicit localization strategy was adopted to ameliorate the spurious long-range correlations (for more details see Tian *et al.* [2011] and Tian and Xie [2012]).

2.3. WRF-PODEN3DVar

[22] In this system, the 3rd nested initial file named “wrfinput_d03” was updated by the results from PODEn3DVar, where the initial variables of the WRF model are linked to Doppler radar observation by observation operators and the cost function through the POD method. The updated initial variables include x-wind, y-wind, z-wind, perturbation temperature, perturbation pressure, rainwater mixing ratio, water-vapor mixing ratio, and cloud-water mixing ratio. The rain gauge data indicated that there were two precipitation events on June 21, 2008; one was from 05 to 06 UTC, and the other was from 07 to 10 UTC. The whole data assimilation time window is from 01 to 06 UTC. The ensemble model state samples are generated by WRF simulation at a certain data assimilation time with 103 different initial conditions from June 19, 00 UTC, to June 23, 06 UTC, for the first assimilation procedure, and the time interval is set to one hour. Therefore, their corresponding simulated-observation samples can be obtained by applying the observation operator to the ensemble model state ensemble. As a result, the MPs are then obtained by the model state ensemble minus the background state vector (which is obtained by running the WRF-ARW model hourly by taking the analysis fields at the time step an hour ago as the initial fields). Correspondingly, their OPs can also be achieved through the simulated-observation ensemble minus the background simulated-observation vector (applying the observation operator to the background model state). The background error covariance can be also updated through $\mathbf{P}_b = \frac{\mathbf{P}_x \mathbf{P}_x^T}{N-1}$ and $\mathbf{X}^a = \mathbf{P}_x \left[(N-1) \mathbf{P}_a^* \right]^{\frac{1}{2}}$. Furthermore, a localization radius with 10 grid points is set in this PODEn3DVar system through sensitivity experiments.

3. Experimental Design

[23] Four groups of data are prepared, including rain gauge data, precipitation retrieval data based on Doppler radar,

Table 1. WRF Model Physical Configuration in This Study

Physics Processes	Domain 1 (25 km)	Domain 2 (5 km)	Domain 3 (1 km)
Horizontal	20×20	30×30	50×50
Time interval	150 s	30 s	6 s
Microphysics	Lin et al. scheme	Lin et al. scheme	Lin et al. scheme
Cumulus Parameterization	Kain-Fritsch scheme	Kain-Fritsch scheme	None
PBL	YSU scheme	YSU scheme	YSU scheme
Radiation	Dudhia scheme	Dudhia scheme	Dudhia scheme
Surface-Land	Noah LSM	Noah LSM	Noah LSM
Initial and Boundary data	NCEP / FNL analysis	1st domain	2nd domain

WRF simulation and traditional WRF-3DVar assimilating Doppler radar observation, to compare with the Doppler radar assimilation by WRF-PODEN3DVar. A description of WRF-PODEN3DVar has been addressed, and brief introductions to these four groups are given in the following sections. Doppler radar observation data preprocessing is also described here.

3.1. WRF Configuration

[24] The model's physical configuration is given in Table 1, and the nesting domains and locations of the Doppler radar and gauges are shown in Figure 1. The number of model vertical layers can be freely specified and is 27 in this system. A description of the WRF is presented in Skamarock *et al.* [2008]. The model is initialized by real boundary conditions using NCAR-NCEP's Final Analysis (FNL) data [*U. S. National Centers for Environmental Prediction*, 2009], with a resolution of $1^\circ \times 1^\circ$ every six hours.

3.2. WRF-3DVar

[25] In this study, traditional WRF-3DVar [Barker *et al.*, 2004] for Doppler radar reflectivity and radial velocity assimilation was performed. The dynamical and physical configuration remained same as for the WRF simulation. The first guess x^b is an hour short-rang ARW forecast by cycling mode. The background error (BE) covariance is generated by the National Meteorological Center (NMC)-CV5 (local statistics method for WRF) method [Parrish and Derber, 1992] with $(T + 24)$ minus $(T + 12)$ forecasting difference, and the input data for statistically generating BE are WRF ensemble forecasts from May 21, 2008, to June 21, 2008. The BE length scaling parameter was 0.5, and the BE variance was 0.25 for all variables.

3.3. Doppler Radar Observation Data

[26] This experiment, as part of the Watershed Airborne Telemetry Experimental Research (WATER; a detailed introduction to WATER is given by Li *et al.* [2008, 2009]) project, was carried out on June 21, 2008, in Minle County of Gansu Province. A dual-polarization Doppler weather radar with X-band was used in our experiment. This radar was developed by the Cold and Arid Regions Environmental and Engineering Research Institute of Chinese Academic Sciences. It uses a high-gain, low-sidelobe polarization antenna, dual power feeders, a high-power solid-state modulator klystron transmitter, dual low-noise high dynamic linear receivers, a high-precision digital IF processor, dual-polarization Doppler signal processing and display terminals. Its beam width is 1° , the number of bins is 1000, the bin

length is from 50 m to 250 m, the volume scan number is 23, and the time interval is around 15 min. In this experiment, the radar was located at 38.72°N , 100.65°E , at an elevation of 1669.0 m. Figures 2a and 2b show the difference displays of radar reflectivity and radial velocity for periods of no rain and heavy rain, respectively.

[27] The preprocessing of the original Doppler radar data before they were assimilated into the WRF-PODEN3DVar system in this study includes (1) erasing folded velocity and clutter for radial velocity, (2) smoothing for radar reflectivity and radial velocity, and (3) interpolating and gridding for radar reflectivity and radial velocity. The *James and Houze* [2001] algorithm was adopted to erase folded velocity and clutter, The *Barnes* [1964] scheme was used to interpolate three-dimensional radar data from measured points to the model setting with resolution of 1000 m in the horizontal dimensions and 27-layer in the model's vertical dimension. Figure 3 shows the difference between pre- and post-data preprocessing for radar reflectivity and radial velocity in the model's first layer at 08:30 UTC on June 21, 2008. It is obvious that there is much noise in the original radar reflectivity and radial velocity, and the data after preprocessing are much smoother. There were weak Doppler radial velocity and reflectivity before 04 UTC on June 21, 2008. They gradually became stronger from 05 to 09 UTC, and then to 11 UTC, gradually becoming weaker until they disappeared. In order to illustrate this developing process, the time interval for gridded radar reflectivity maps and radial velocity maps is a half hour in Figure 4 and Figure 5 in the model's first vertical layer. The time period is from 05 to 11 UTC, June 21, 2008.

3.4. Precipitation Retrieval Based on Doppler Radar Observation

[28] The following retrieval algorithm was given by Zhao *et al.* [2011] for the rainfall rate from Doppler radar data:

$$P_r = 0.198 * K_{DP}^{0.4405} * 10^{(0.035 * Z - 0.036 * Z_{DR})} \quad (19)$$

where P_r is the rainfall rate (units of mm/h), K_{DP} is the specific differential phase, Z is the reflectivity, and Z_{DR} is the differential reflectivity. The rainfall rate from 00:00 to 15:00 on June 21, 2008, is shown in Figure 6.

3.5. Gauge Data

[29] To provide validation data for Doppler radar data assimilation in WRF-PODEN3DVar, 9 HOBO Data Logging Rain Gauges were distributed in the research region. The gauges are named R01, R02, R03, R04, R05, R06, R07, R08

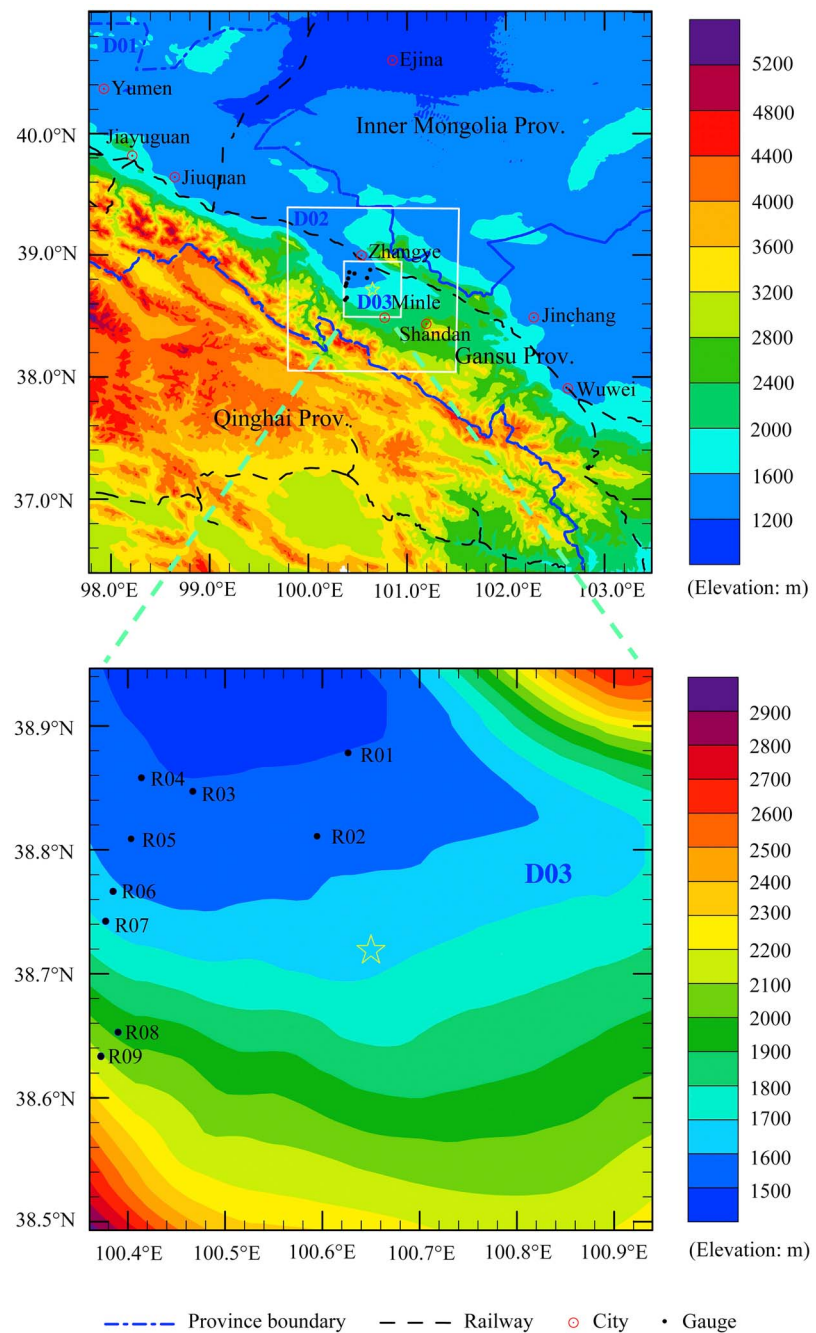


Figure 1. Nesting domain configuration for the numerical experiment (a black dot means a gauge site, and a yellow star means a Doppler radar site).

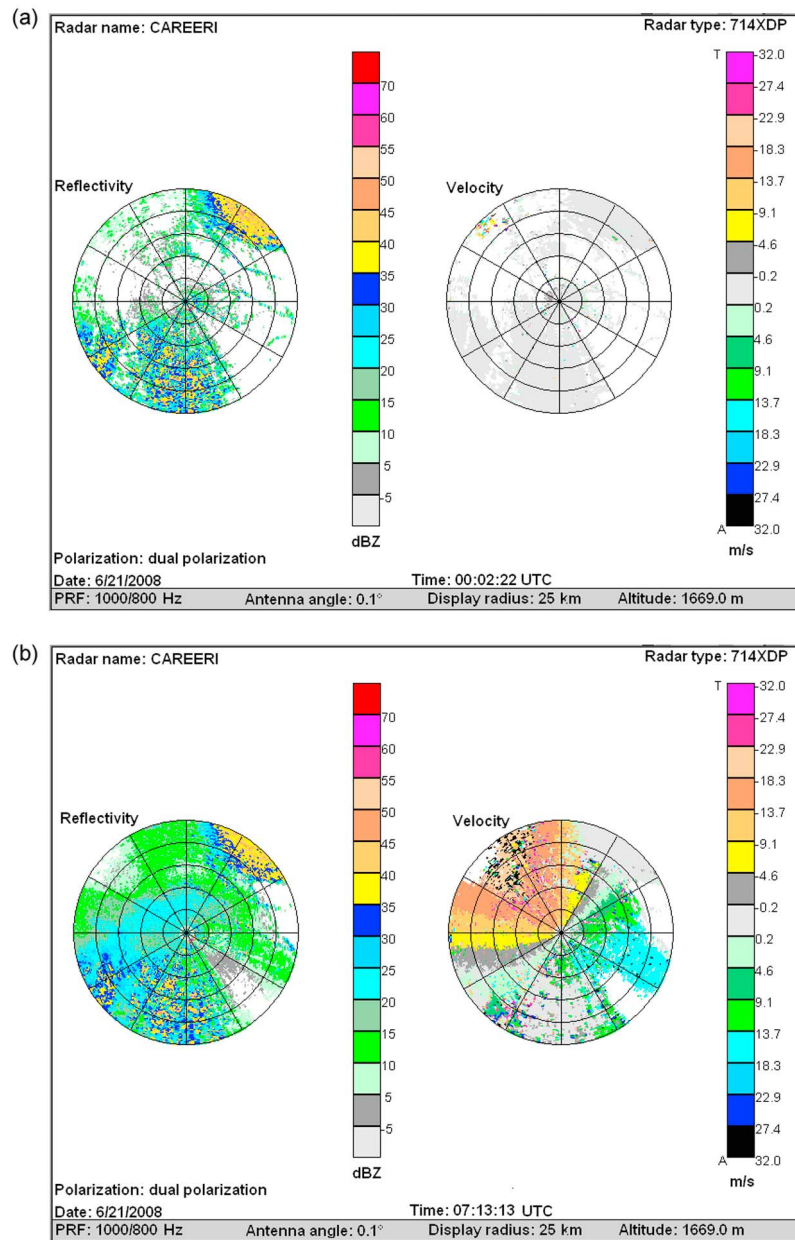


Figure 2. Maps of Doppler radar reflectivity and velocity at (a) 00:02:22 and (b) 07:13:13 on June 21, 2008.

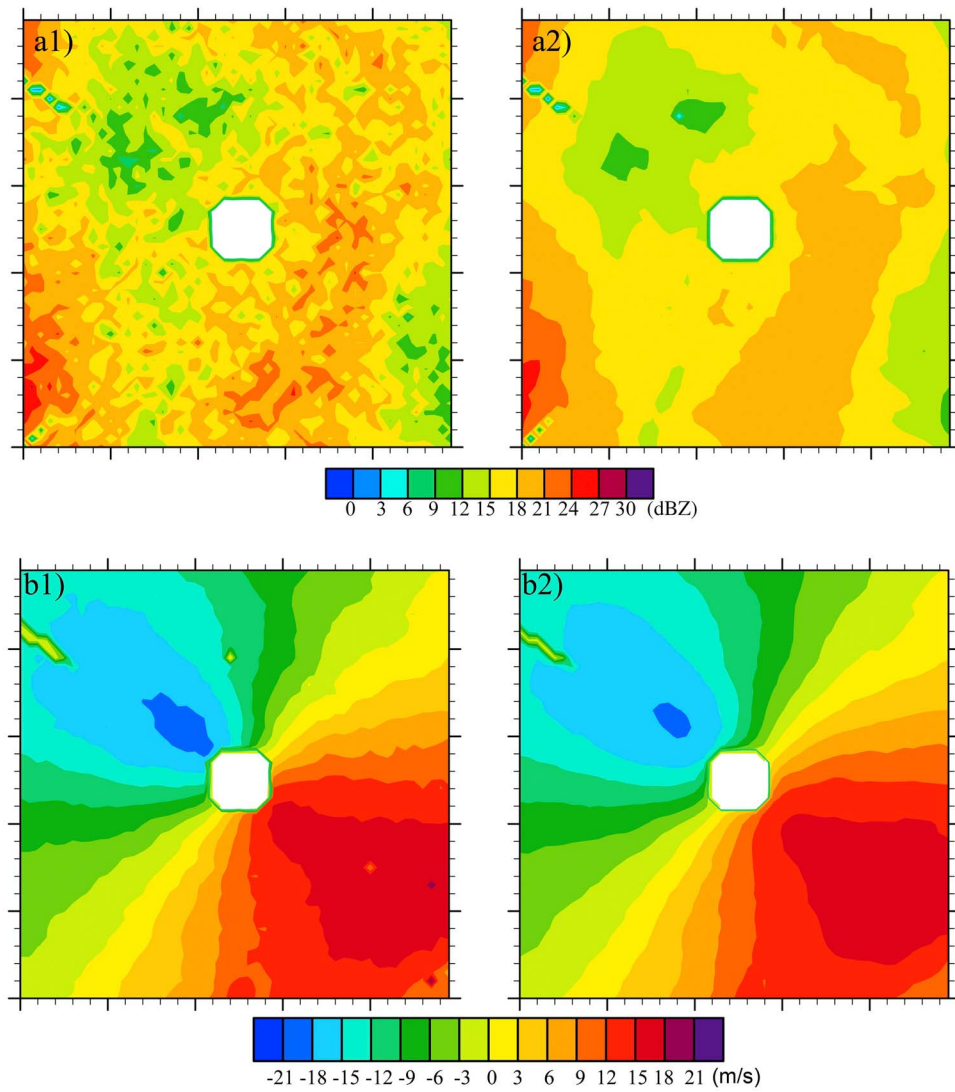


Figure 3. Pre- and post-data-preprocessing for radar data on June 21, 08:30 UTC, 2008.

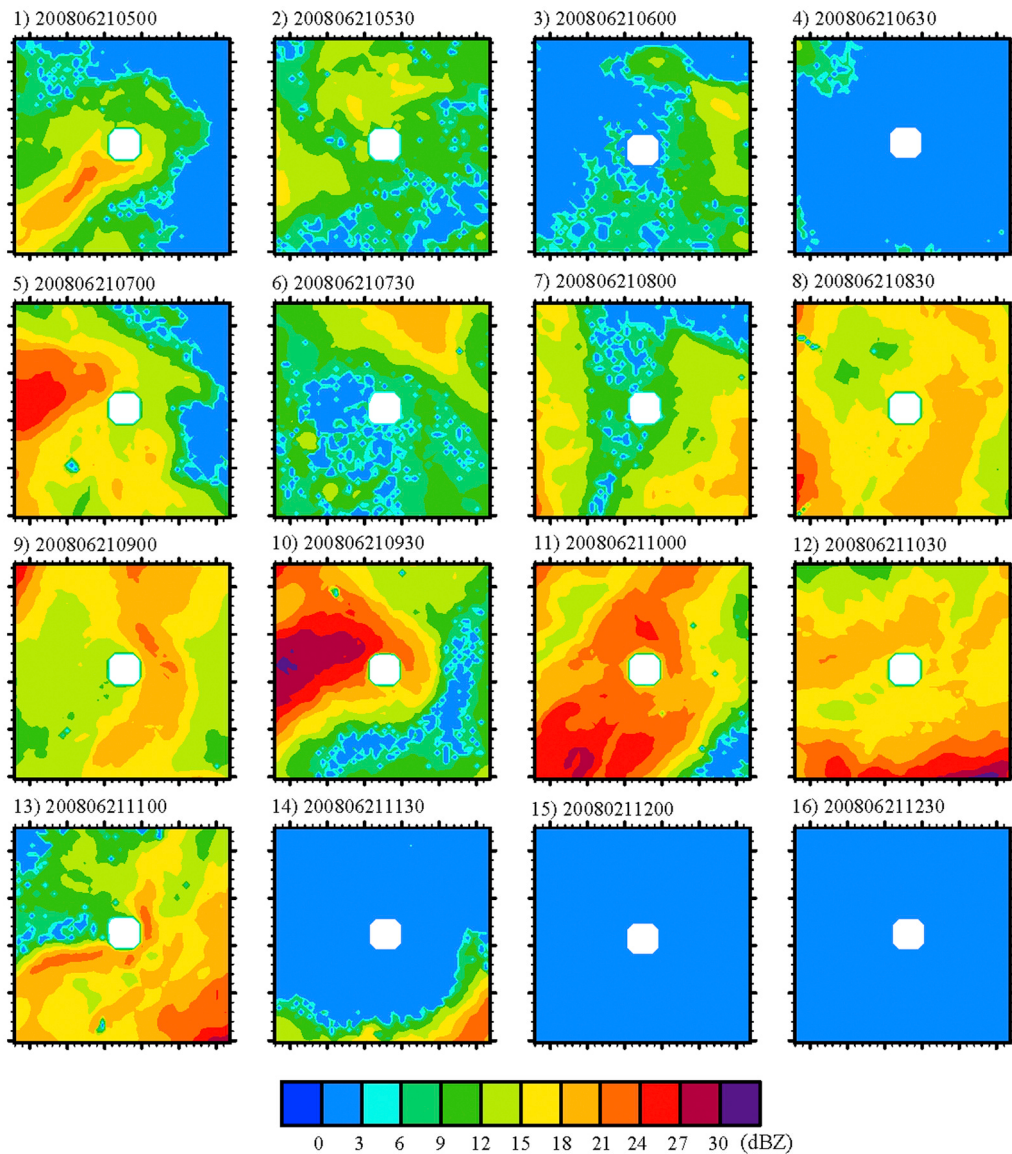


Figure 4. Gridded Doppler radar reflectivity maps at the 1st model vertical layer from 05:00 to 12:30 on June 21, 2008, at half-hour intervals (units of dBZ).

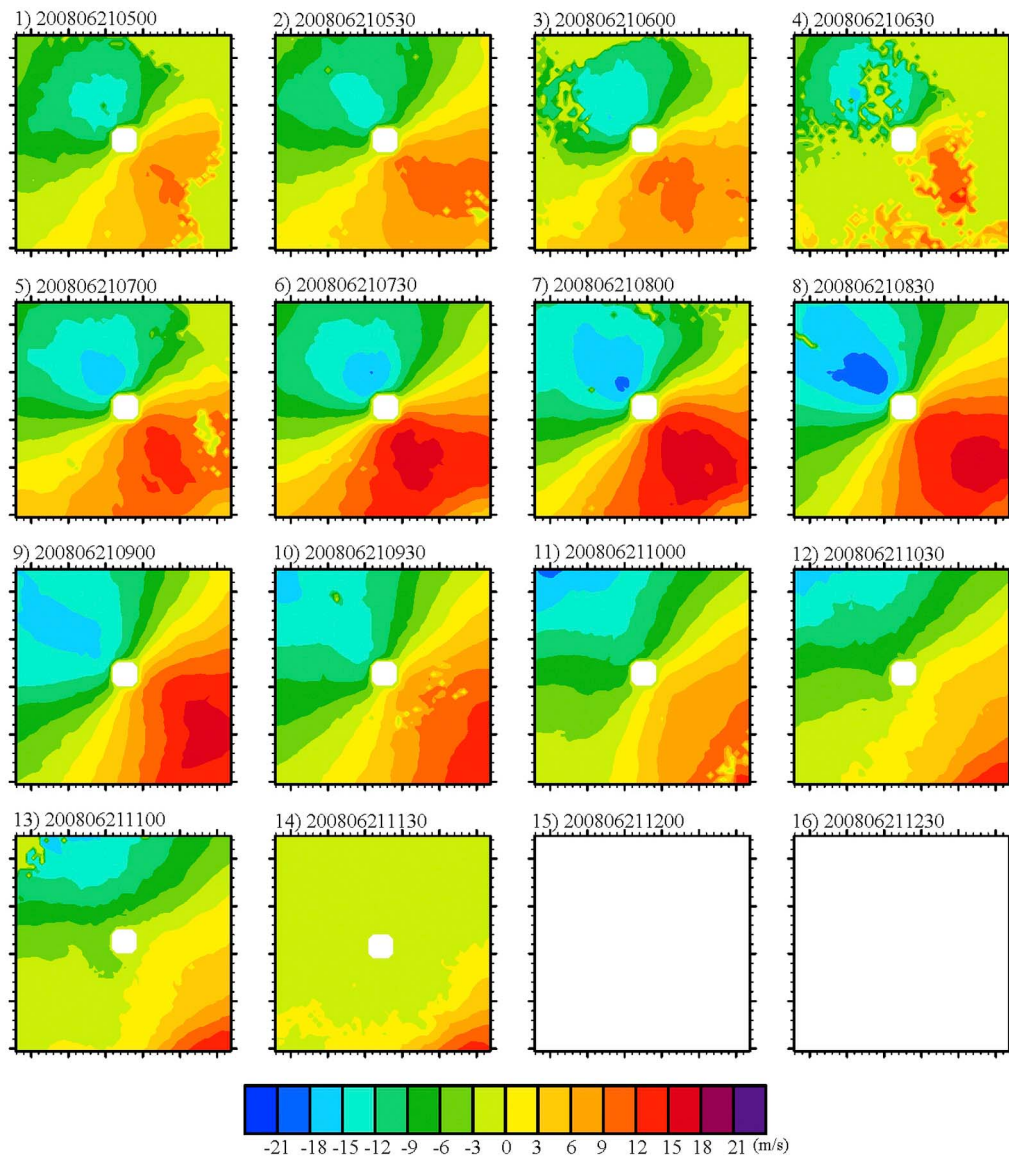


Figure 5. Gridded Doppler radial-velocity maps at the 1st model vertical layer from 05:00 to 12:30 on June 21, 2008, at half-hour intervals (units of m/s).

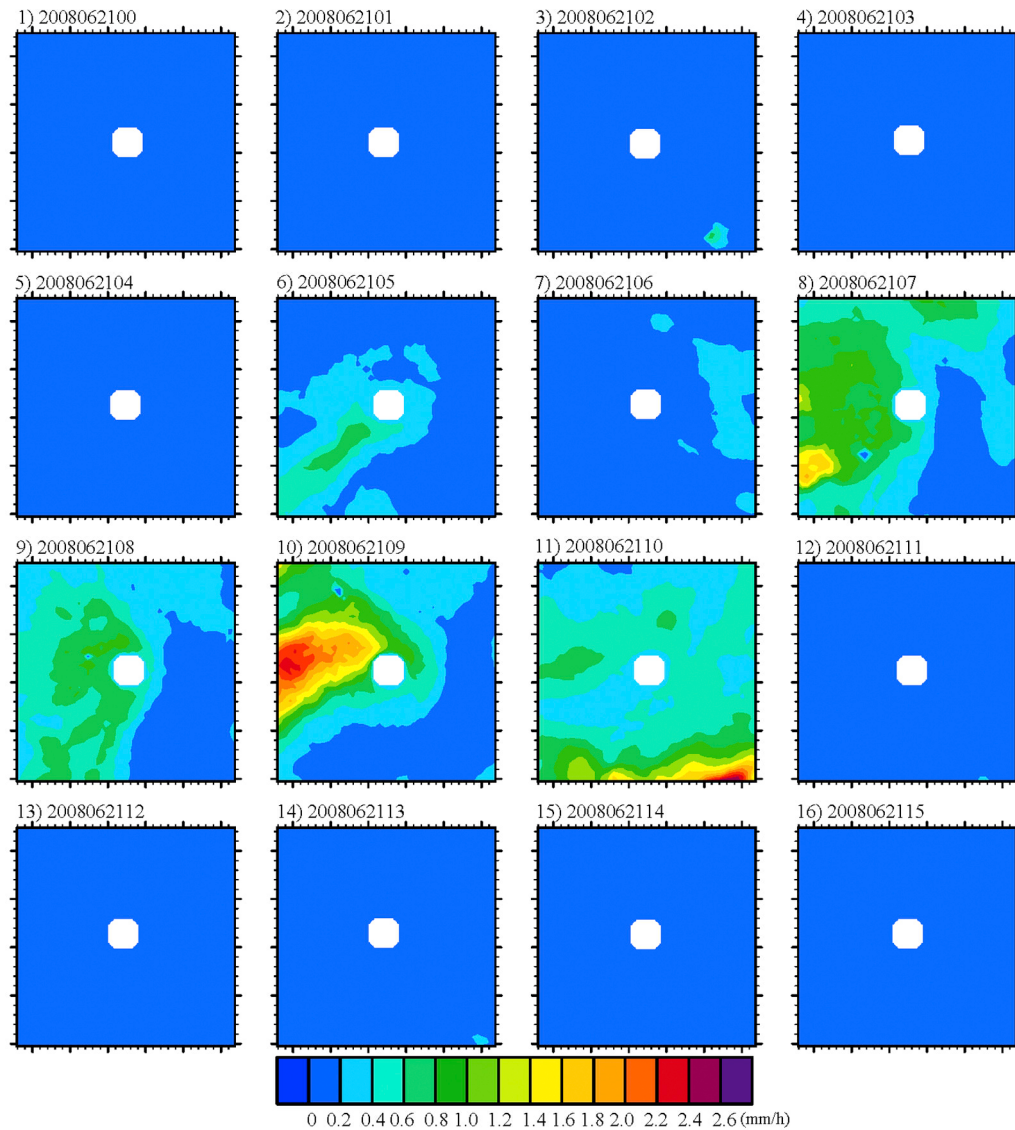


Figure 6. Retrieval rainfall rate from 00:00 to 15:00, at 1-h intervals (units of mm/h).

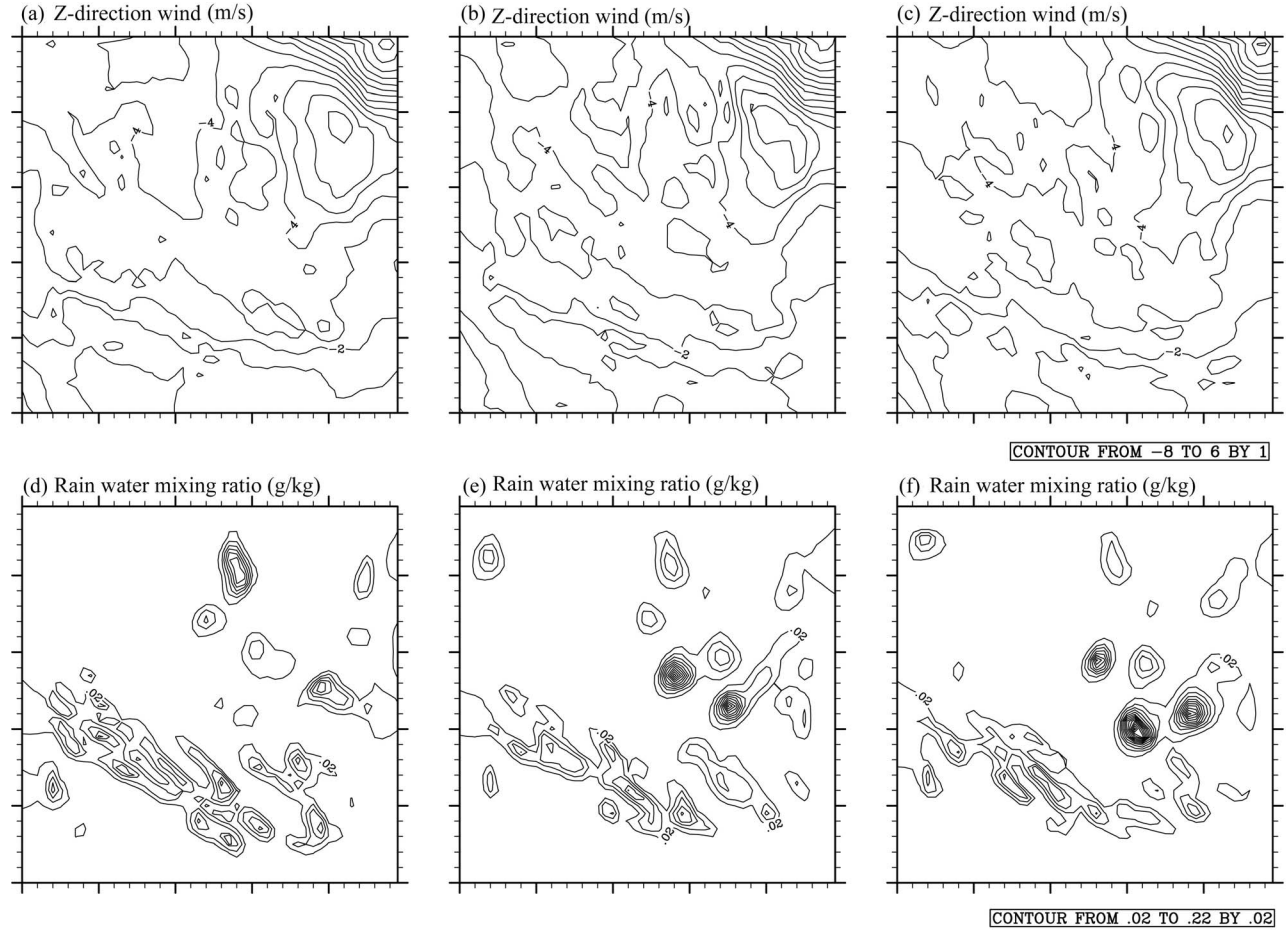


Figure 7. Wind contours and rainwater-mixing-ratio contours demonstrating the sensitivity to the initial ensemble sizes at the 9th model vertical layer: (a, b and c) Z-direction wind for the sizes of 80, 103 and 120, respectively, with units of m/s; (d, e, and f) rainwater mixing ratio for the sizes of 80, 103 and 120, respectively, with units of g/kg.

and R09. The exact locations of these gauges are given in Figure 1.

4. WRF-PODEN3DVar Sensitivity Analyses and Single-Observation Test

4.1. Analysis of Sensitivity to the Initial Ensemble Size

[30] The initial ensemble size and the selection of the initial ensemble members are two important issues in using ensembles of discrete forecasting to approximate the evolution of an initial probability distribution in a model [Anderson, 1996]. Atmospheric processes have the characteristic of time continuity, so the selection of initial ensemble members for the WRF model is a focus in WRF forecasting during pre- and post-analysis times. The size of the initial ensemble is 103 in our study, and two comparison groups are set as 80 and 120 for the analysis of sensitivity to the initial ensemble size. Figure 7 displays wind contours and rainwater-mixing-ratio contours demonstrating the analysis of sensitivity to the initial ensemble size for values of 80, 103 and 120 in the 9th vertical layer of the model. The wind contours for three ensemble sizes are similar and have no significant

differences among them. However, the rainwater-mixing-ratio contours for an initial ensemble size of 80 is a little different from those for sizes of 103 and 120. The rainwater-mixing-ratio contours for sizes of 103 and 120 are similar, so it is reasonable to take 103 as the initial ensemble size in our study.

4.2. Analysis of Sensitivity to Localization

[31] Localization is a means to improve sampling error when small ensembles are used to sample the statistical relations between an observation and a state variable [Anderson, 2007]. It is essential to apply localization to large models that contain many state variables. A localization radius of 10 grid points is used in our study, and the two compared groups are set as 8 grid points and 12 grid points. Figure 8 displays wind contours and rainwater-mixing-ratio contours for localization radii of 8, 10 and 12 grid points in the 9th vertical layer of the model. Figures 8a, 8b and 8c display the Z-direction wind fields, which all have similar patterns with strong wind speeds in the northeast portion of the 3rd domain, although in the south portion, the Z-wind simulated with a localization radius of 10 grid points is very

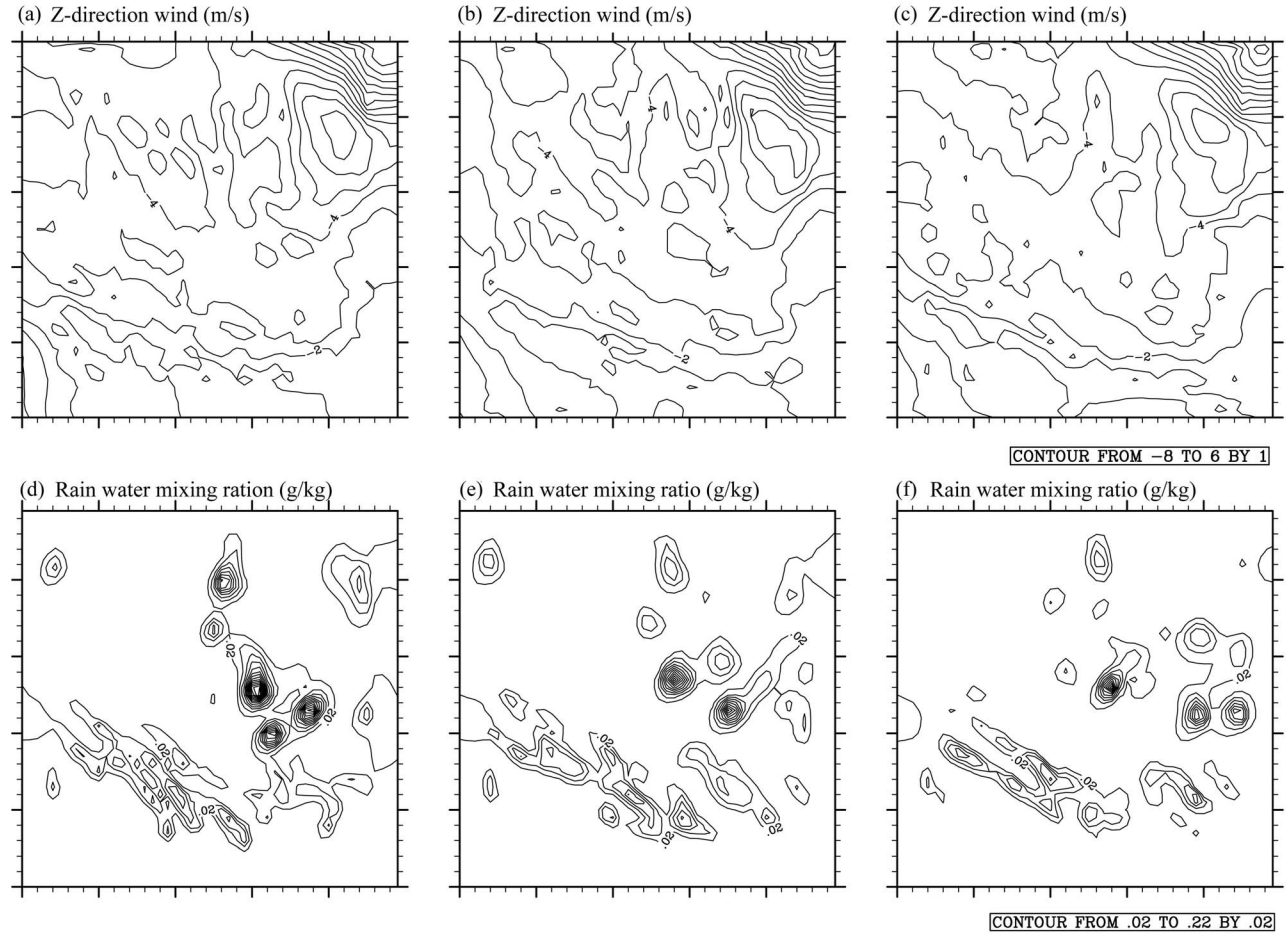


Figure 8. Wind contours and rainwater-mixing-ratio contours demonstrating the sensitivity to the localization radius at the 9th model vertical layer: (a, b, and c) Z-direction wind for radii of 8, 10 and 12 grid points, respectively, with units of m/s; (d, e, and f) rainwater mixing ratio for radii of 8, 10 and 12 grid points, respectively, with units of g/kg.

similar to that with a localization radius of 8 grid points. Figures 8d, 8e and 8f show the rainwater-mixing-ratio fields for different simulations with different localization radii. The rainwater-mixing-ratio contour distributions simulated by WRF-PODEn3DVar with localization radii of 8, 10 and 12 grid points are alike, though the contours simulated with a 12-grid point radius are a little sparser than the others. Therefore, the localization radius of 10 grid points adopted in this study is reasonable.

4.3. Single-Observation Test

[32] Before the real-data experiment, a single-radial-velocity test was executed for WRF-3DVar and WRF-PODEn3DVar. In the single-observation test, one radial velocity was set to 15 m/s at the grid point location (9, 25, 25), which is the location relative to the total (27, 50, 50). The first dimension is the model vertical layer (9/27), the second dimension is latitude (25/50), and the last dimension is longitude (25/50). Figures 9a and 9b illustrate the increments of Z-direction wind and temperature by WRF-3DVar at the 9th model vertical layer, respectively, Figures 9c and 9d are by WRF-PODEn3DVar accordingly. Comparison of Figures 9c and 9d with Figures 9a and 9b indicates that the increments

contours of Z-direction wind and temperature are within the localization radius and the spreading is more uniform by WRF-PODEn3DVar than WRF-3DVar. This test shows that our PODEn3DVar is effective and can be applied to real-data cases.

5. Results and Discussion

5.1. Initial Variable Increments

[33] Figure 10 includes comparison plots of rainwater mixing ratios at the 9th model vertical layer from 01 to 06 UTC on June 21, 2008, among WRF simulation, WRF-3DVar assimilation and WRF-PODEn3Var assimilation. Rainwater mixing ratios from 01 to 06 UTC simulated by the WRF-PODEn3DVar system show a strong aggregation in the southeast portion of the 3rd domain. The results of the WRF simulation are irregular. The WRF-PODEn3DVar simulation yields higher rainwater mixing ratios than the WRF simulation or the WRF-3DVar assimilation. The horizontal wind fields show that a cyclone was forming, and there was a gradual increase in the rainwater mixing ratio field from 01 UTC to 06 UTC in the WRF-PODEn3DVar assimilation. Apparently, there is a larger change in wind fields

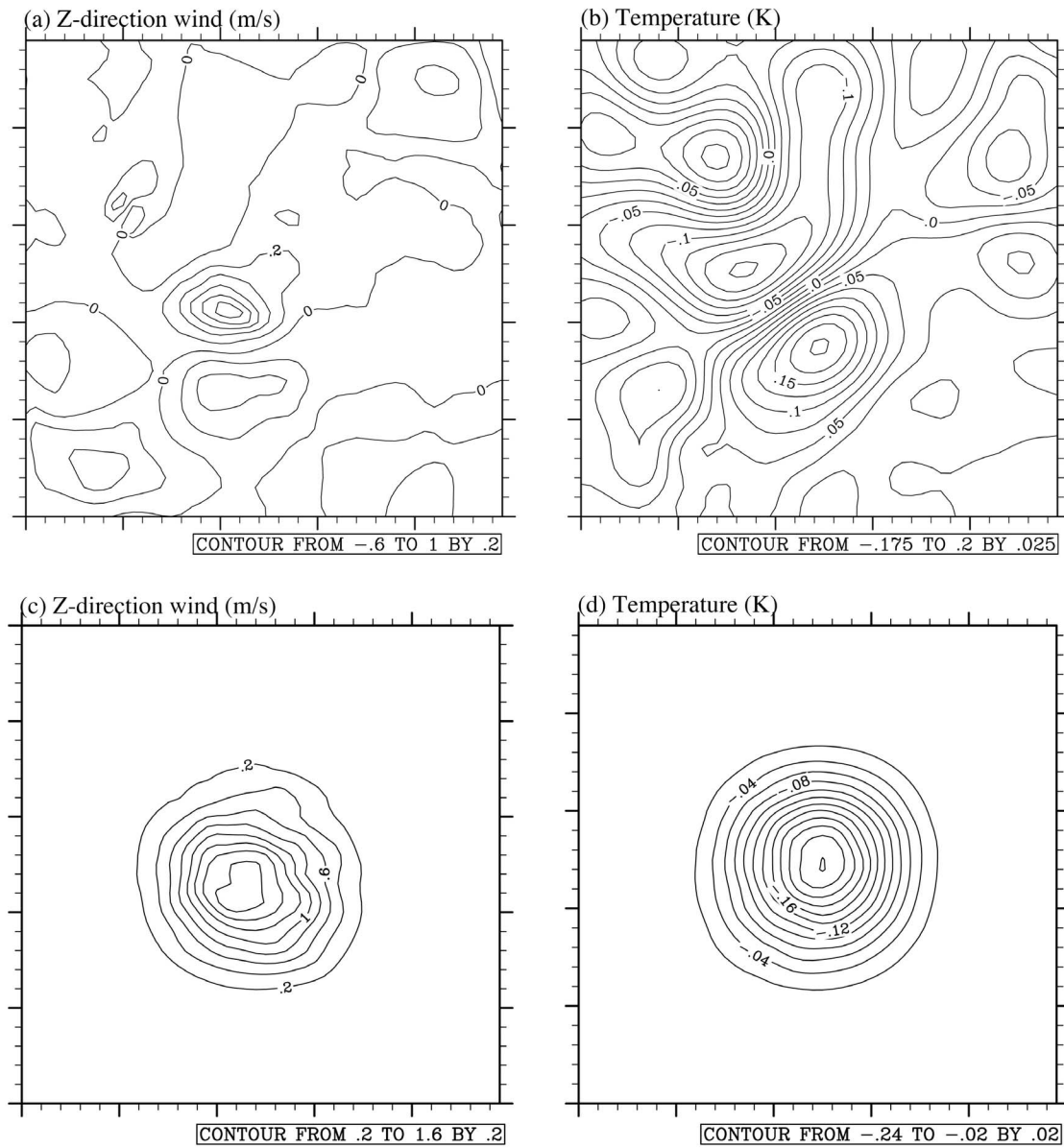


Figure 9. Wind contours and temperature contours demonstrating the application of the increments to a single radial-velocity (15 m s^{-1}) observation relative to the radar at the 9th model vertical layer: (a) Z-direction wind increment by WRF-3DVAR (m s^{-1}); (b) temperature increment by WRF-3DVAR (m s^{-1}); (c) Z-direction wind increment by WRF-3DVar (K); (d) temperature increment by WRF-PODEN3DVar (K).

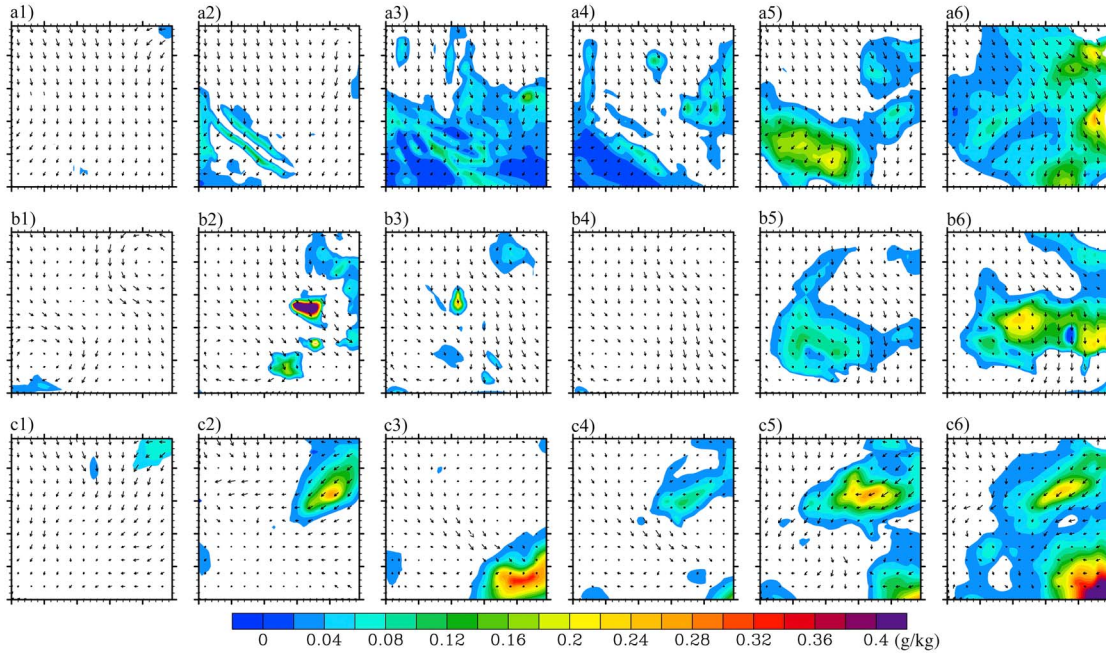


Figure 10. Rainwater mixing ratio overlaid with horizontal wind fields at the 9th model vertical layer on June 21, 2008. (a1–a6) WRF simulation from 01 UTC to 06 UTC; (b1–b6) WRF-3DVar assimilation from 01 to 06 UTC; (c1–c6) WRF-PODEN3DVar assimilation from 01 UTC to 06 UTC.

between the WRF-3DVar assimilation and the WRF simulation. However, there is not so obvious a change in the rainwater mixing ratio in the WRF-3DVar assimilation. The difference is possibly caused by moisture spinup, which is still an unresolved problem in the WRF-3DVar [Lee *et al.*, 2006] and limits the accuracy of rainfall forecasting in the early period of the Doppler radar-observation data assimilation. Another possibility is that the difference is due to the state BE covariance in the WRF-3DVar system.

[34] In Figure 11, differences in rainwater mixing ratio, temperature and geopotential height between WRF-PODEN3DVar assimilation and WRF simulation are shown for 06 UTC, June 21, 2008, at the 3rd, 6th and 9th model vertical layers. Overall, rainwater mixing ratio increases, especially in the southeast. Temperature decreases in the northeast and increases in the southwest at the 3rd and 6th model vertical layers. Rainwater mixing ratio and temperature both increase at the 9th model vertical layer, especially in the southeast. Geopotential height increases in the southwest portion of the 3rd domain and decreases in the northeast portion, especially at the 9th model vertical layer.

[35] Figure 12 illustrates the vertical profiles of Doppler radar reflectivity and differences in initial variables (rainwater mixing ratio, temperature and geopotential height); 1: WRF-PODEN3DVar assimilation minus WRF simulation, 2: WRF-3DVar assimilation minus WRF simulation) from the 1st to the 20th model vertical layers on 06 UTC, June 21, 2008. Figure 12a is the observation reflectivity. The top panels in Figures 12b, 12d and 12f are rainwater mixing ratio, temperature and geopotential height difference between the WRF-PODEN3DVar and WRF simulations, the bottom panels in Figures 12c, 12e and 12g are differences between the WRF-3DVar and WRF simulations. The profile patterns of rainwater mixing ratio in the two panels of Figures 12b

and 12c are almost the same; however, Figure 12b has a much stronger contrast between the east portion and west portion. Finally, the two panels of Figures 12d and 12e have the same profile pattern of temperature, but Figure 12d has a much higher absolute value than Figure 12e. The profile patterns of geopotential height are different. Figure 12g shows small negative values over almost the whole profile, and there is a contrast between south and north in Figure 12f. There are high values of radar reflectivity in the east and, accordingly, an obvious increase in rainwater mixing ratio and centers of decreasing temperature and geopotential height in the east below the 10th layer; from the 10th to the 20th model vertical layers, neither radar reflectivity nor rainwater mixing ratio has significant changes. Increases in the geopotential height and the temperature are obvious at the layers above the 10th layer, and there is a center of strongly increasing values in the east and of weakly decreasing values in the west for rainwater mixing ratio. The pattern is just the opposite for temperature.

[36] Figures 10–12 show the rainwater mixing ratio simulated by is higher than that by WRF and WRF-3DVar, the vertical difference profile of rainwater ratio (WRF-PODEN3DVar simulation minus WRF simulation) is more similar to observation reflectivity. These indicate that the initial conditions provided by WRF-PODEN3DVar are reasonable and better than those by WRF and WRF-3DVar.

5.2. Forecasting Results

[37] Figures 13 and 14 are the curve and the chart for accumulated rainfall during the period from 00 UTC to 15 UTC comparing rain observation, Doppler radar retrieval, WRF simulation, WRF-3DVar assimilation and WRF-PODEN3DVar assimilation at 9 rain gauges. Rainfall simulated and forecasted by the WRF model (in blue color) is far

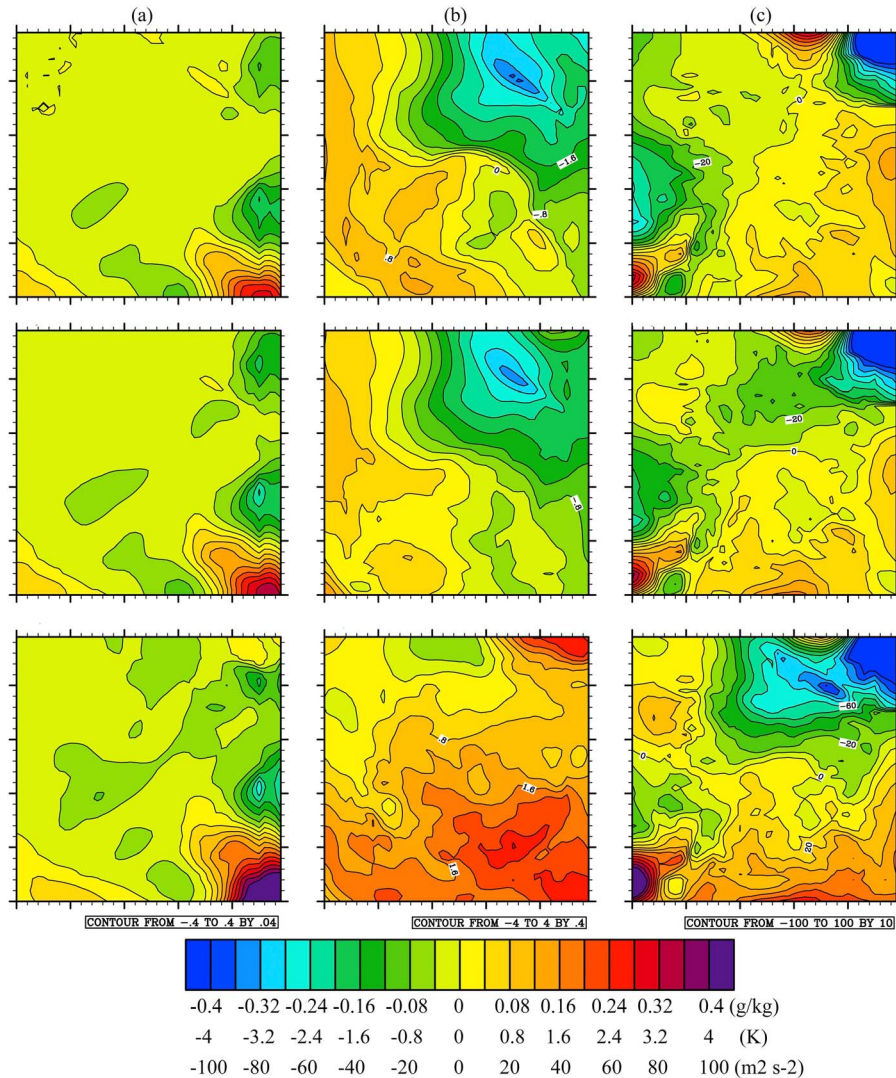


Figure 11. Initial variable differences (WRF-PODEN3DVar assimilation minus WRF simulation) at 06 UTC, June 21, 2008 (a) increments of rainwater mixing ratio for the 3rd, 6th and 9th model vertical layer, respectively, units of g/kg; (b) increments of temperature for the same model layers, units of K; (c) increments of geopotential height for the same model layers, units of m^2/s^2 .

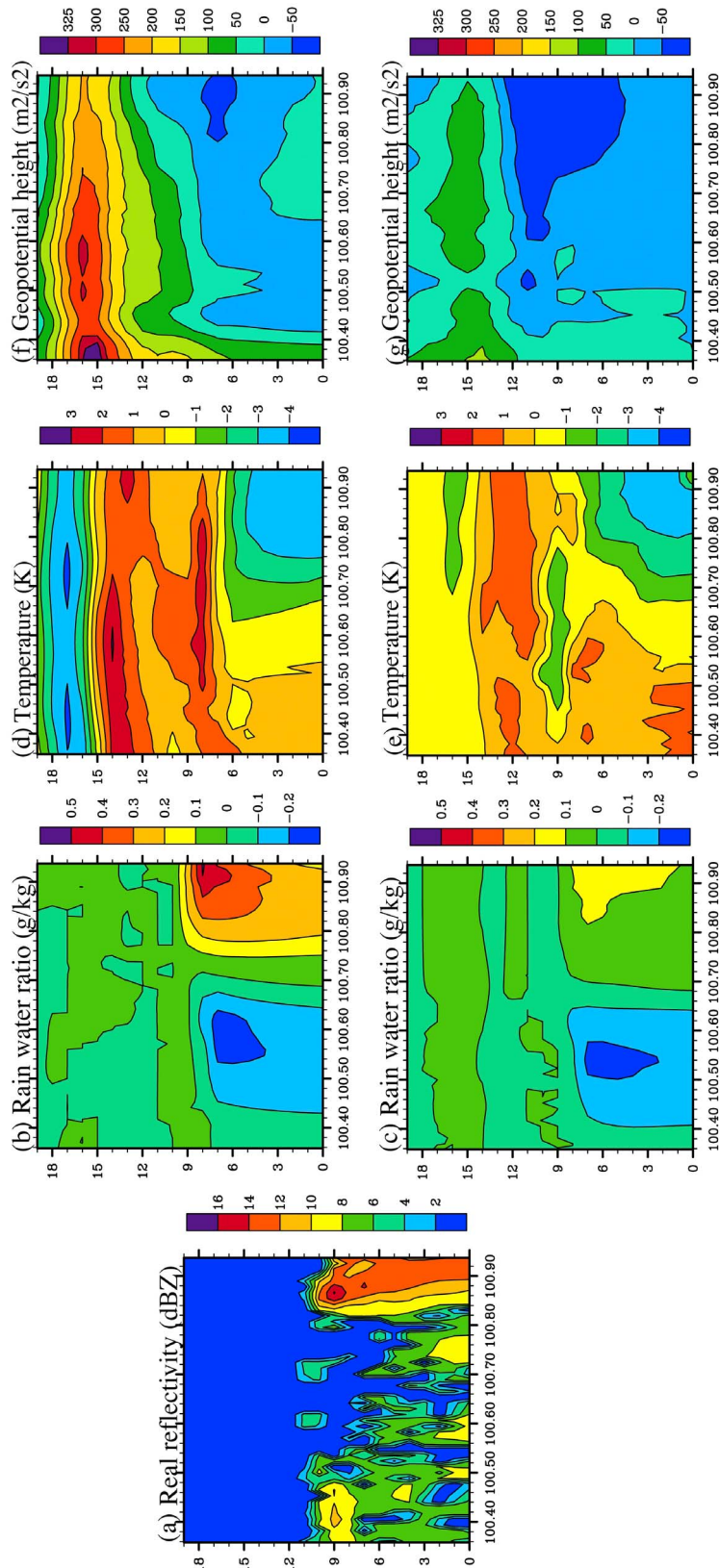


Figure 12. Vertical profiles (the 1st to the 20th model vertical layer) of observation reflectivity and initial variable differences. (b, d, and f) WRF-PODEN3DVar simulation minus WRF simulation; (c, e, and g) WRF-3DVar simulation minus WRF simulation through 38.5°N at 06 UTC, June 21, 2008. (a) Observation reflectivity (units of dBZ); (b and c) increment of QRAIN (units of g/kg); (d and e) increment of temperature (units of K); (f and g) increment of geopotential height (units of m²/s²).

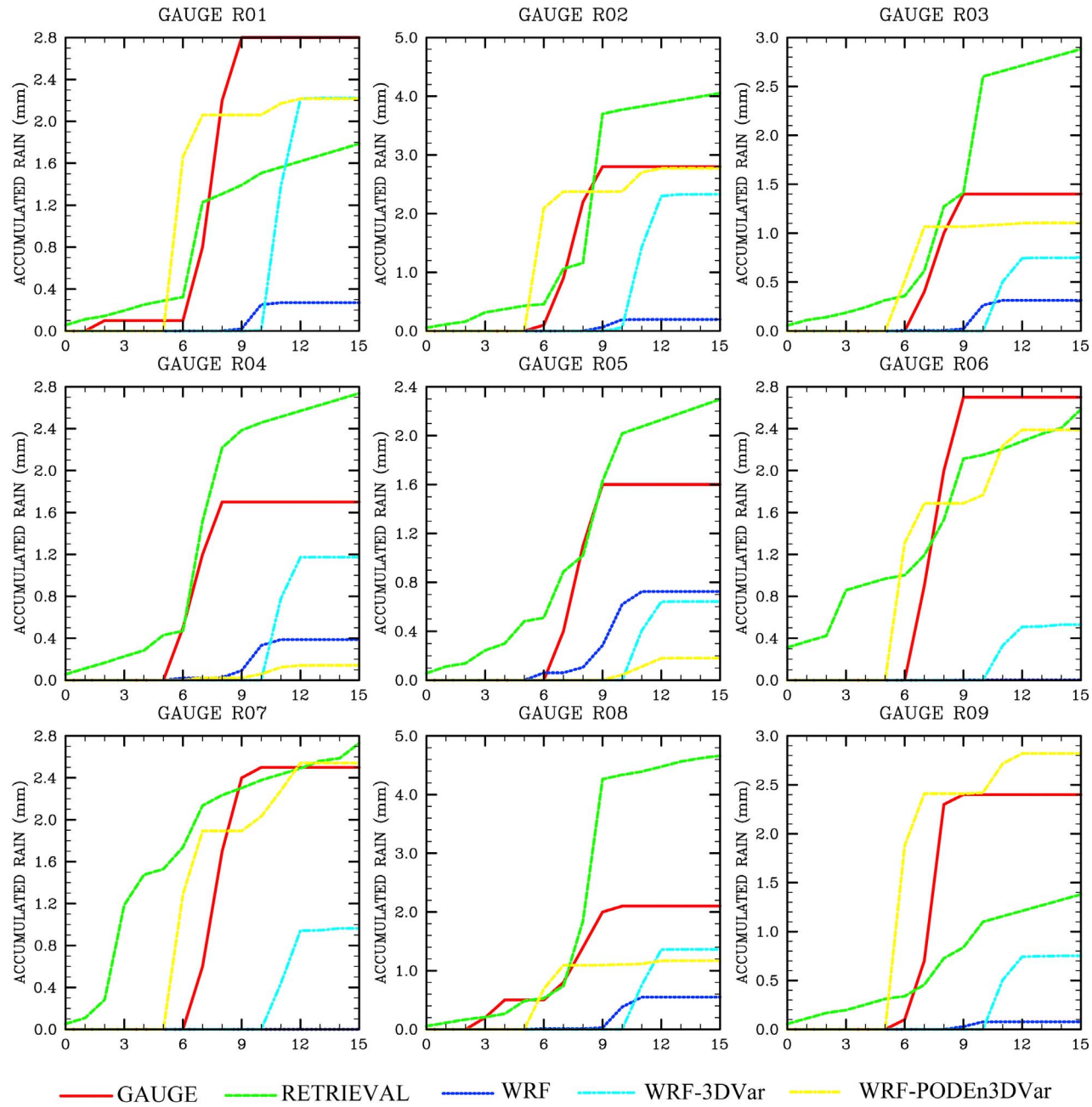


Figure 13. Comparisons of accumulated rainfall curves for Doppler radar retrieval, WRF simulation, WRF-3DVar, WRF-PODEN3DVar and gauge observations (time period is from 00 UTC to 15 UTC).

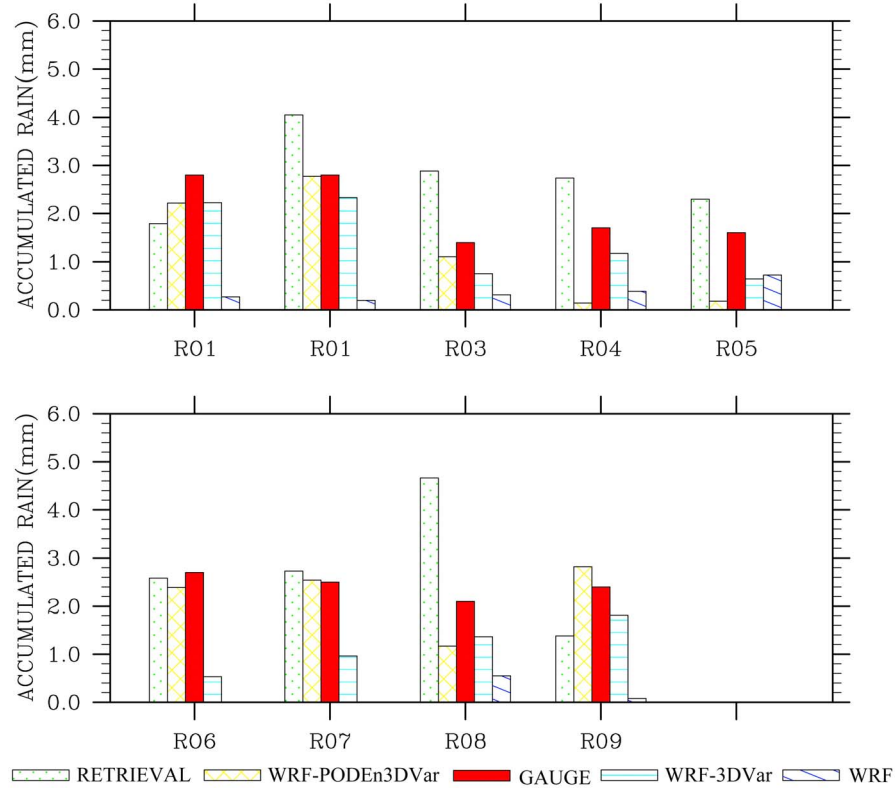


Figure 14. Same as Figure 13 but in chart form.

lower than the observation. Rainfall assimilated and forecasted by WRF-PODEN3DVar agrees well with observation data at the R01, R02, R03, R06, R07 and R08 gauges. Correspondingly, possibly because of spinup problems, there are almost no precipitation fluxes from 00 UTC to 10 UTC in the WRF-3DVar assimilation at the gauge sites; however, the precipitation fluxes sharply increase from 11 UTC to 13 UTC, and the accumulated volumes of rainfall assimilated and forecasted by WRF-3DVar are far higher than the WRF model's, though the volumes are lower than those of the rain gauges and WRF-PODEN3DVar. The accumulated volumes of rainfall retrieved by Doppler radar observation data in equation (12) also agree well with the rain gauges, especially at R06 and R07. Normally, the retrieval rainfall rates are

higher than the rain gauges, especially at R08, which is located at the edge of a mountain (see Figure 1), has a strong reflectivity at 09 UTC (see Figure 4), and shows a high rainfall rate at 09 UTC (see Figure 6). Apparently, the much higher accumulated rainfall volume at R08 is derived from the above sequent "higher"; however, a reasonable explanation is that the wrong information is implied in the data pre-processing of radar reflectivity when applied to a complex mountainous region.

[38] Table 2 illustrates the accumulated rainfall and error estimate. Compared with the gauge data, the average error of accumulated rainfall volumes from the WRF simulation at the gauge sites is 0.28 mm, which is much lower than the average of the gauge observations (2.22 mm). The average of

Table 2. Rain-Rate-Error Statistics Between Doppler Retrieval, WRF Simulation, WRF-3DVar and WRF-PODEN3DVar^a

Gauge Number	Gauge	Accumulated Rainfall (mm)				Retrieval (mm/h)		WRF (mm/h)		WRF-3DVar (mm/h)		PODEN3DVar (mm/h)	
		Retrieval	WRF	WRF-3DVar	WRF-PODEN3DVar	MBE	RMSE	MBE	RMSE	MBE	RMSE	MBE	RMSE
R01	2.80	1.79	0.27	2.22	2.50	-0.06	0.36	-0.16	0.57	-0.04	0.58	-0.02	0.42
R02	2.80	4.05	0.20	2.33	3.50	0.08	0.58	-0.16	0.41	-0.03	0.58	0.04	0.63
R03	1.40	2.88	0.31	0.75	1.20	0.09	0.31	-0.07	0.21	-0.04	0.25	-0.01	0.22
R04	1.70	2.74	0.39	1.17	0.28	0.07	0.17	-0.08	0.25	-0.03	0.33	-0.09	0.25
R05	1.60	2.30	0.73	0.64	0.29	0.04	0.19	-0.16	0.23	-0.06	0.26	-0.08	0.24
R06	2.70	2.58	0.01	0.53	2.40	-0.01	0.30	-0.10	0.47	-0.14	0.41	-0.02	0.40
R07	2.50	2.73	0.00	0.96	2.78	0.01	0.39	-0.15	0.36	-0.10	0.40	0.02	0.08
R08	2.10	4.66	0.55	1.36	2.46	0.16	0.48	-0.07	0.29	-0.05	0.34	0.02	0.25
R09	2.40	1.38	0.08	0.75	4.06	-0.06	0.36	-0.17	0.60	-0.06	0.45	0.10	0.43
AVG	2.22	2.79	0.28	1.19	2.16	0.04	0.35	-0.12	0.38	-0.06	0.40	0.00	0.32

^aMBE: mean bias error, RMSE: root-mean square error.

Table 3. The 2×2 Contingency Tables Between Rain Gauge and Doppler Retrieval, WRF Simulation, WRF-3DVar, and WRF-PODEN3DVar^a

Rain Gauge	Retrieval		WRF		WRF-3DVar		WRF-PODEN3DVar		
	Yes	No	Yes	No	Yes	No	Yes	No	SUM
Yes	22	12	16	18	0	34	25	9	34
No	19	91	9	101	18	92	10	100	110
SUM	41	103	25	119	18	126	35	109	144

^aYes if rainfall ≥ 0.1 mm/h, otherwise No.

accumulated rainfall volume from the WRF-PODEN3Var assimilation at the gauge sites is 2.16 mm, which is much closer to the average gauge observation. They are 0.28 mm and 1.19 mm for WRF simulation and WRF-3DVar assimilation. However, the rainfall simulation and forecasting were affected by spinup problems. The Doppler radar assimilation in WRF-3DVar plays an important role in improving the determination of accumulated rainfall volume, though the accumulated rainfall volume is only half that of the rain gauges. The mean bias errors (MBEs) of rainfall rate (unit of mm/s) for radar retrieval, WRF simulation, WRF-3DVar assimilation and WRF-PODEN3DVar assimilation are 0.04, -0.12 , -0.06 and 0.00, respectively. The root-mean square errors (RMSEs) are 0.35 mm/h, 0.38 mm/h, 0.40 mm/h and 0.32 mm/h, respectively.

[39] The 2×2 contingency tables among rain gauge, Doppler radar retrieval, WRF simulation, WRF-3DVar assimilation and WRF-PODEN3DVar assimilation were built (Table 3). In this table, “Yes” is set if rain rate ≥ 0.1 mm/h; otherwise “No” is set to avoid “Yes” for Doppler radar retrieval every hour, at some of which the rain rate is bitty. The time period is from 00 UTC to 15 UTC, the time interval is 1 h, and the number of rain gauges is 9. Thus, the number of total analysis times is 144, and the number of raining times is 34 h. The scalar attributes [Wilks, 2006] characterizing 2×2 contingency tables are probability of detection (POD), threat score (TS), false alarm ratio (FAR), frequency bias (B or FBI) and equitable threat score (ETS). The higher the values of POD, TS and ETS are, the better the simulation or retrieval is; the lower FAR is, the better the simulation or retrieval is; and the closer to 1 FBI is, the better the simulation of retrieval is. The results from the calculation of these scalar attributes are shown in Table 4. Values of POD (with a threshold of rainfall rate ≥ 0.1 , the same as for other indicators) are 0.65, 0.47, 0.00 and 0.74 for Doppler radar retrieval, WRF simulation, WRF-3DVar assimilation and WRF-PODEN3DVar assimilation, respectively. Values of TS are 0.42, 0.37, 0.00 and 0.57, respectively. Values of FAR are 0.46, 0.36, 1.00 and 0.29, respectively. Values of FBI are 1.21, 0.74, 0.53 and 1.03, respectively. Values of ETS are 0.28, 0.27, -0.09 and 0.46, respectively. With threshold ≥ 0.1 mm/h, it is apparent that WRF-PODEN3DVar assimilation yields the highest values of POD, TS and ETS, the lowest value of FAR and an FBI value closer to 1. Figure 15 shows the trend curves for POD, TS, FAR, FBI and ETS across a range of rainfall-rate thresholds from 0.1 mm/h to 0.8 mm/h. Rainfall simulated and forecasted by WRF-3DVar is zero during the rainfall period (from 05 UTC to 09 UTC), values of PC and TS are zero, values of FAR are highest and reach 1, and values of ETS are lowest and almost 0 for all thresholds. Rainfall rate simulated by WRF is far

lower than that of the rain gauges, except for a threshold of 0.1 mm/h. Values of POD, TS, FAR and ETS of WRF are the same as those of WRF-3DVar; however, the FBI is much worse than that of WRF-3DVar because rainfall rate simulated by WRF is too small to reach the threshold (>0.1 mm/h). With the threshold increases, the values of FBI from WRF-3DVar are steady, close to that of Doppler radar retrieval and near 0.6. The results from WRF-PODEN3DVar are comparable to those of Doppler radar retrieval for POD, TS and ETS. FARs estimated from WRF-PODEN3DVar are lower than those from Doppler radar retrieval. FBIs from WRF-PODEN3DVar are a little higher than those from Doppler radar retrieval.

[40] Figures 13–15 indicates that WRF-PODEN3DVar yields better precipitation forecasting than WRF and WRF-3DVar.

5.3. Discussion

[41] Doppler radar data are assimilated in the WRF model by two methods. One is the traditional 3DVar, and the other is PODEN3DVar. As far as WRF-PODEN3DVar is concerned, the value of the rainwater mixing ratio (refer to Figure 10) from WRF-PODEN3DVar is higher than from the WRF simulation. Similarly, the value of the rainfall rate simulated (refer to Figures 13 and 14) by WRF-PODEN3DVar is far higher than that from the WRF simulation. From Table 2, it can be found that the accumulated rainfall volume yielded by the WRF-PODEN3DVar simulation is closer to the observation data than that by the WRF simulation, which is far lower than the rain gauge observations. Rainfall-event verification metrics also show that the WRF-PODEN3DVar assimilation is much better than the WRF simulation. For WRF-3DVar, there is a large change in the wind fields, though there is almost no improvement for the rainwater mixing ratio. The latter phenomenon is possibly due to the spinup problem in WRF-3DVar. The accumulated rainfall volume estimated by WRF-3DVar is clearly improved over the WRF simulation, though the improvement is limited and the accumulated rainfall volume is only half that of the rain

Table 4. Verification for Doppler Radar Retrieval, WRF Simulation, WRF-3DVar and WRF-PODEN3DVar by Rain Gauge^a

	POD	TS	FAR	FBI	ETS
Retrieval	0.65	0.42	0.46	1.21	0.28
WRF	0.47	0.37	0.36	0.74	0.27
WRF-3DVar	0.00	0.00	1.00	0.53	-0.09
WRF-PODEN3DVar	0.74	0.57	0.29	1.03	0.47

^aRainfall ≥ 0.1 mm/h. POD: probability of detection (different from proper orthogonal decomposition), TS: threat score, FAR: false alarm ratio, FBI: frequency bias, ETS: equitable threat score.

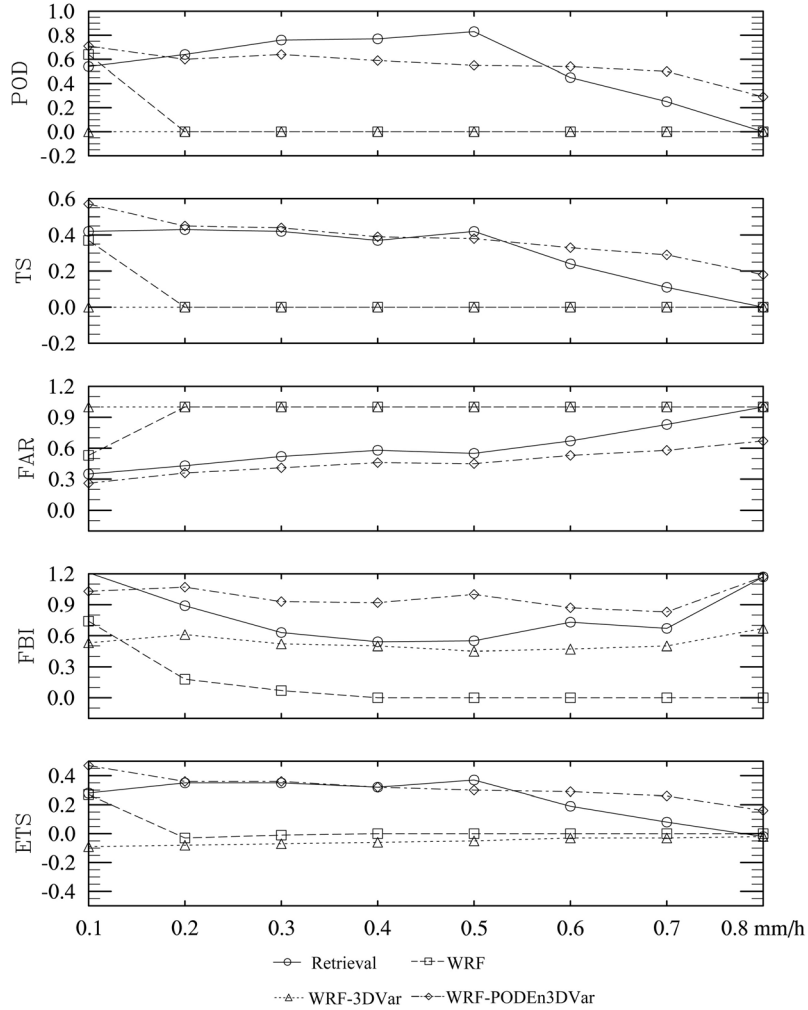


Figure 15. Verification metrics trend curves across the rainfall thresholds arranged from 0.1 mm/h to 0.8 mm/h.

gauges. A possible reason is that WRF-3DVar uses the state BE in the whole assimilation time window. Based on the results of the Doppler radar assimilation in WRF-PODEN3DVar and WRF-3DVar, it is certain that it is effective in improving the initial condition for the WRF model by assimilating the Doppler radar observation data.

[42] The WRF model initialized by NCEP GFS-fnl data is difficult to graph for the finer-scale weather processes in complex mountainous regions. Even more significant, rainfall simulated by the WRF model is also affected by spinup problems, which limit the accuracy of rainfall forecasting by WRF-3DVar. There are many approaches [Lynch and Huang, 1992; Grell *et al.*, 1995; Bloom *et al.*, 1996; Benjamin *et al.*, 2004; Lee *et al.*, 2006] for reducing spinup effects on the WRF-3DVar system. These approaches are not used in this paper, so (1) there is a large change for wind fields and almost no improvement for rainwater mixing ratio by WRF-3DVar assimilation compared with WRF simulation, and (2) rainfall verification shows poor results for WRF simulation and WRF-3DVar assimilation. Because flow-dependent covariances developed from the ensemble of short-range forecasts minus background state vector are provided in the WRF-PODEN3DVar system, the spinup

problem is greatly reduced, and the rainwater mixing ratio simulated by WRF-PODEN3DVar is greatly improved. It is thus helpful for the WRF model to reduce the spinup problem using WRF-PODEN3DVar to assimilate the Doppler radar observation data.

6. Conclusions

[43] This study investigated the performance of Doppler radar assimilation on the capability of forecasting rainfall in the WRF model based on PODEn3DVar. The following conclusions can be drawn:

[44] 1. Assimilating the Doppler radar radial velocity and reflectivity can effectively improve the description of the 3-dimensional structures in the initial conditions for the WRF model.

[45] 2. It is effective to assimilate Doppler radar-reflectivity and radial-velocity observations in the WRF model by PODEn3DVar.

[46] 3. Compared with WRF-3DVar, flow-dependent covariances developed from the ensemble of short-range forecasts minus background state vector provided in WRF-PODEN3DVar are more helpful in reducing the spinup

problem in the WRF model and avoiding a state BE in the assimilation time windows.

[47] 4. Comparisons of the accumulated rainfall volumes and the verification scalars, including POD, TS, FAR, FBI and ETS, indicate that WRF-PODEN3DVar simulation yields better rainfall forecasting than radar retrieval, and radar retrieval is better than WRF-3DVar assimilation. The worst performer is WRF simulation.

[48] **Acknowledgments.** This work was supported by the CAS Action Plan for West Development Program (grant KZCX2-XB3-15) and by grants from the National Natural Science Foundation of China (40901202, 40925004 and 40875063). The Doppler radar data and rain gauge data used in this paper were obtained from the WATER experiment (<http://westdc.westgis.ac.cn/water>). The input data for the WRF model are from the Research Data Archive (RDA), which is maintained by the Computational and Information Systems Laboratory (CISL) at the National Center for Atmospheric Research (NCAR). The original data are available from the RDA (<http://dss.ucar.edu>) in data set number ds083.2. The authors thank three anonymous reviewers and the editor for their very helpful comments.

References

- Anderson, J. L. (1996), Selection of initial conditions for ensemble forecasts in a simple perfect model framework, *J. Atmos. Sci.*, **53**(1), 22–36, doi:10.1175/1520-0469(1996)053<0022:SOICFE>2.0.CO;2.
- Anderson, J. L. (2007), Exploring the need for localization in ensemble data assimilation using a hierarchical ensemble filter, *Physica D*, **230**(1–2), 99–111, doi:10.1016/j.physd.2006.02.011.
- Barker, D. M., W. Huang, Y. R. Guo, and Q. N. Xiao (2004), A three-dimensional (3DVAR) data assimilation system for use with MM5: Implementation and initial results, *Mon. Weather Rev.*, **132**, 897–914, doi:10.1175/1520-0493(2004)132<0897:ATVDAS>2.0.CO;2.
- Barnes, L. (1964), A technique for maximizing details in numerical weather map analysis, *J. Appl. Meteorol.*, **3**, 396–409, doi:10.1175/1520-0450(1964)003<0396:ATFMDI>2.0.CO;2.
- Benjamin, S. G., D. Dévényi, S. S. Weygandt, K. J. Brundage, J. M. Brown, G. A. Grell, D. Kim, B. E. Schwartz, T. G. Smirnova, and T. L. Smith (2004), An hourly assimilation-forecast cycle: The RUC, *Mon. Weather Rev.*, **132**, 495–518, doi:10.1175/1520-0493(2004)132<0495:AHACTR>2.0.CO;2.
- Bloom, S. C., L. L. Takacs, A. M. da Silva, and D. Ledvina (1996), Data assimilation using incremental analysis updates, *Mon. Weather Rev.*, **124**, 1256–1271, doi:10.1175/1520-0493(1996)124<1256:DAUIAU>2.0.CO;2.
- Daescu, D. N., and I. M. Navon (2007), Efficiency of a POD-based reduced second-order adjoint model in 4D-Var data assimilation, *Int. J. Numer. Methods Fluids*, **53**, 985–1004, doi:10.1002/fld.1316.
- Dowell, D., F. Zhang, L. Wicker, C. Snyder, B. Skamarock, and A. Crook (2002), Wind and thermodynamic retrievals in a supercell thunderstorm: Ensemble Kalman filter results, paper presented at 19th Conference on Weather Analysis and Forecasting, Am. Meteorol. Soc., San Antonio, Tex.
- Fang, F., C. C. Pain, I. M. Navon, M. D. Piggott, G. J. Gorman, P. Allison, and A. J. H. Goddard (2009), A POD reduced order 4D-VAR adaptive mesh ocean modeling approach, *Ocean Modell.*, **60**, 709–732, doi:10.1002/fld.1911.
- Gal-Chen, T. (1978), A method for the initialization of the anelastic equations: Implications for matching models with observation, *Mon. Weather Rev.*, **106**(5), 587–606, doi:10.1175/1520-0493(1978)106<0587:AMFTIO>2.0.CO;2.
- Grell, G. A., J. Dudhia, and D. R. Stauffer (1995), A description of the fifth-generation Penn State/NCAR mesoscale model (MM5), *NCAR Tech. Note NCAR/TN-398+STR*, 122pp., NCAR, Boulder, Colo.
- James, C. N., and R. A. Houze (2001), A real-time four-dimensional Doppler dealiasing scheme, *J. Atmos. Oceanic Technol.*, **18**, 1674–1683, doi:10.1175/1520-0426(2001)018<1674:ARTFDD>2.0.CO;2.
- Kapitza, H. (1991), Numerical experiments with the adjoint of a non-hydrostatic mesoscale model, *Mon. Weather Rev.*, **119**, 2993–3011, doi:10.1175/1520-0493(1991)119<2993:NEWTAO>2.0.CO;2.
- Lee, M. S., Y. H. Kuo, D. M. Barker, and E. Lim (2006), Incremental analysis updates initialization technique applied to 10-km MM5 and MM5 3DVar, *Mon. Weather Rev.*, **134**, 1389–1404, doi:10.1175/MWR3129.1.
- Li, X., et al. (2008), Simultaneous remote sensing and ground-based experiment in the Heihe River Basin: Scientific objectives and experiment design, *Adv. Earth Sci.*, **23**(9), 897–914.
- Li, X., et al. (2009), Watershed allied telemetry experimental research, *J. Geophys. Res.*, **114**, D22103, doi:10.1029/2008JD011590.
- Lynch, P., and X. Y. Huang (1992), Initialization of the HIRLAM model using a digital filter, *Mon. Weather Rev.*, **120**, 1019–1034, doi:10.1175/1520-0493(1992)120<1019:IOTHMU>2.0.CO;2.
- Meischner, P. (2005), *Weather Radar: Principles and Advanced Applications*, 354 pp., Springer, New York.
- Michalakes, J., J. Dudhia, D. Gill, J. Klemp, and W. Skamarock (1999), Design of a next-generation regional weather research and forecast model, in *Towards Teracomputing: Proceedings of the Eighth ECMWF Workshop on the Use of Parallel Processors in Meteorology*, edited by W. Zwiefelhofer, pp. 117–124, World Sci., Hackensack, N. J.
- Michalakes, J., S. Chen, J. Dudhia, L. Hart, J. Klemp, J. Middlecoff, and W. Skamarock (2001), Development of a next generation regional weather research and forecast model, in *Developments in Teracomputing: Proceedings of the Ninth ECMWF Workshop on the Use of High Performance Computing in Meteorology*, edited by W. Zwiefelhofer and N. Kreitz, pp. 269–276, World Sci., Hackensack, N. J.
- Michalakes, J., J. Dudhia, D. Gill, T. Henderson, J. Klemp, W. Skamarock, and W. Wang (2005), The Weather Research and Forecast Model: Software architecture and performance, in *Proceedings of the 11th ECMWF Workshop on the Use of High Performance Computing in Meteorology*, edited by W. Zwiefelhofer and G. Mozdynski, pp. 156–168, World Sci., Hackensack, N. J.
- Parrish, D. F., and J. C. Derber (1992), The National Meteorological Center's spectral statistical interpolation analysis system, *Mon. Weather Rev.*, **120**, 1747–1763, doi:10.1175/1520-0493(1992)120<1747:TNSMCSS>2.0.CO;2.
- Skamarock, W. C., J. B. Klemp, and J. Dudhia, D. O. Gill, D. M. Barker, M. G. Duda, X. Y. Huang, W. Wang, and J. G. Powers (2008), A description of the advanced research WRF version 3, 226pp., NCAR, Boulder, Colo. [Available at www.mmm.ucar.edu/wrf/users/docs/user_guide/ARWUsersGuide.pdf.]
- Snyder, C., and F. Zhang (2003), Assimilation of simulated Doppler radar observations with an ensemble Kalman filter, *Mon. Weather Rev.*, **131**, 1663–1677, doi:<http://dx.doi.org/10.1175//2555.1>.
- Sun, J., and N. A. Crook (1994), Wind and thermodynamic retrieval from single-Doppler measurements of a gust front observed during Phoenix II, *Mon. Weather Rev.*, **122**, 1075–1091, doi:10.1175/1520-0493(1994)122<1075:WATRFS>2.0.CO;2.
- Sun, J., and N. A. Crook (1997), Dynamical and microphysical retrieval from Doppler radar observations using a cloud model and its adjoint. Part I: Model development and simulated data experiments, *J. Atmos. Sci.*, **54**, 1642–1661, doi:10.1175/1520-0469(1997)054<1642:DAMRFD>2.0.CO;2.
- Sun, J., and N. A. Crook (1998), Dynamical and microphysical retrieval from Doppler radar observations using a cloud model and its adjoint. Part II: Retrieval experiments of an observed Florida convective storm, *J. Atmos. Sci.*, **55**, 835–852, doi:10.1175/1520-0469(1998)055<0835:DAMRFD>2.0.CO;2.
- Sun, J., D. Flicker, and D. Lilly (1991), Recovery of three-dimensional wind and temperature fields from simulated single-Doppler radar data, *J. Atmos. Sci.*, **48**, 876–890, doi:10.1175/1520-0469(1991)048<0876:ROTDWA>2.0.CO;2.
- Tian, X., and Z. Xie (2012), Implementations of a square-root ensemble analysis and a hybrid localization into the POD-based ensemble 4DVar, *Tellus, Ser. A*, **64**, 18375, doi:10.3402/tellusa.v64i0.18375.
- Tian, X. J., Z. Xie, and A. Dai (2008), An ensemble-based explicit four-dimensional variational assimilation method, *J. Geophys. Res.*, **113**, D21124, doi:10.1029/2008JD010358.
- Tian, X., Z. Xie, and Q. Sun (2011), A POD-based ensemble four-dimensional variational assimilation method, *Tellus, Ser. A*, **63**(4), 805–816, doi:10.1111/j.1600-0870.2011.00529.x.
- Tong, M., and M. Xue (2005), Ensemble Kalman filter assimilation of Doppler radar data with a compressible nonhydrostatic model: OSS experiments, *Mon. Weather Rev.*, **133**(7), 1789–1807, doi:10.1175/MWR2898.1.
- U.S. National Centers for Environmental Prediction (2009), NCEP FNL Operational model global tropospheric analyses, continuing from July 1999: Dataset ds083.2, <http://dss.ucar.edu/datasets/ds083.2>, NCAR, Boulder, Colo. [Updated daily.]
- Weygandt, S. S., A. Shapiro, and K. K. Droegemeier (2002a), Retrieval of model initial fields from single-Doppler observations of a supercell thunderstorm. Part I: Single-Doppler velocity retrieval, *Mon. Weather Rev.*, **130**, 433–453, doi:10.1175/1520-0493(2002)130<0433:ROMIFF>2.0.CO;2.
- Weygandt, S. S., A. Shapiro, and K. K. Droegemeier (2002b), Retrieval of model initial fields from single-Doppler observations of a supercell thunderstorm. Part II: Thermodynamic retrieval and numerical prediction,

- Mon. Weather Rev.*, 130, 454–476, doi:10.1175/1520-0493(2002)130<0454:ROMIFF>2.0.CO;2.
- Wilks, D. (2006), *Statistical Methods in the Atmospheric Sciences*, 627 pp., Elsevier, New York.
- Wolfsberg, D. (1987), Retrieval of three-dimensional wind and temperature fields from single-Doppler radar data, *CIMMS Rep.* 84, 91 pp., Univ. of Okla., Norman.
- Wu, B., J. Verlinde, and J. Sun (2000), Dynamical and microphysical retrievals from Doppler radar observations of a deep convective cloud, *J. Atmos. Sci.*, 57, 262–283, doi:10.1175/1520-0469(2000)057<0262:DAMRFD>2.0.CO;2.
- Xiao, Q., and J. Sun (2007), Multiple radar data assimilation and short range quantitative precipitation forecasting of a squall line observed during IHOP_2002, *Mon. Weather Rev.*, 135, 3381–3404, doi:10.1175/MWR3471.1.
- Xiao, Q., Y. H. Kuo, J. Sun, W. C. Lee, E. Lim, Y. R. Guo, and D. M. Barker (2005), Assimilation of Doppler radar observation with a regional 3DVAR system: Impact of Doppler velocities on forecasts of a heavy rainfall case, *J. Appl. Meteorol.*, 44, 768–788, doi:10.1175/JAM2248.1.
- Xiao, Q., Y. H. Kuo, J. Sun, W. C. Lee, E. Lim, Y. R. Guo, and D. M. Barker (2007), An approach of radar reflectivity data assimilation and its assessment with the inland QPF of Typhoon Rusa (2002) at landfall, *J. Appl. Meteorol.*, 46, 14–22, doi:10.1175/JAM2439.1.
- Xu, J., Q. Xiao, X. Gao, and S. Sorooshian (2006), Influence of assimilating rainfall derived from WSR-88D radar on the rainstorm forecasts over the southwestern United States, *J. Geophys. Res.*, 111, D13105, doi:10.1029/2005JD006650.
- Zhang, F., C. Snyder, and J. Sun (2004), Impacts of initial estimate and observations on the convective-scale data assimilation with an ensemble Kalman filter, *Mon. Weather Rev.*, 132, 1238–1253, doi:10.1175/1520-0493(2004)132<1238:IOIEAO>2.0.CO;2.
- Zhao, G., R. Chu, T. Zhang, J. Li, J. Shen, and Z. Wu (2011), Improving the rainfall rate estimation in the midstream of the Heihe River Basin using rain drop size distribution, *Hydrol. Earth Syst. Sci.*, 15(3), 943–951, doi:10.5194/hess-15-943-2011.